Powder Technology 470 (2026) 121992

Contents lists available at ScienceDirect

Powder Technology

journal homepage: www.journals.elsevier.com/powder-technology

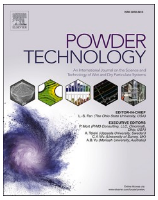

Influence of dispersion gas flow on the spray characteristics and γ-Fe_2O_3 nanoparticles formation and properties in reference SpraySyn burners

Orlando Massopo [a], Ricardo Tischendorf [a], Munko Gonchikzhapov [b], Tina Kasper [b], Peter Augustin [c], Burak Özer [c], Manuel Reddemann [c], Reinhold Kneer [c], Mohammed-Ali Sheikh [d], Aydan Akyildiz Mert [d], Hartmut Wiggers [d,e], Hans-Joachim Schmid [a,*]

[a] Particle Technology Group, Paderborn University, Pohlweg 55, Paderborn, Germany
[b] Technical Thermodynamics, Paderborn University, Pohlweg 55, Paderborn, Germany
[c] Institute of Heat and Mass Transfer, RWTH Aachen, Augustinerbach 6, Aachen, Germany
[d] Institute for Energy and Materials Processes–Reactive Fluids, University of Duisburg-Essen, Carl-Benz-Straße 199, Duisburg, Germany
[e] Center for Nanointegration Duisburg-Essen (CENIDE), University of Duisburg-Essen, Carl-Benz-Straße 199, Duisburg, Germany

HIGHLIGHTS

- SS2 with its angled dispersion gas inlet, provides enhanced atomization and yields finer nanoparticles than SS1.
- Higher dispersion gas flow results in finer droplets, cooler flame, and more compact, less fractal maghemite agglomerates.
- Particle size evolution along the flame centerline of both *SpraySyn* burners are measured by SMPS.
- SS1 exhibits abrupt particle size increase occurring further downstream due to late evaporation and particle recirculation.
- Maghemite agglomerate size is governed by spray flame residence time.
- Guidance for optimizing spray flame synthesis and validating numerical models

GRAPHICAL ABSTRACT

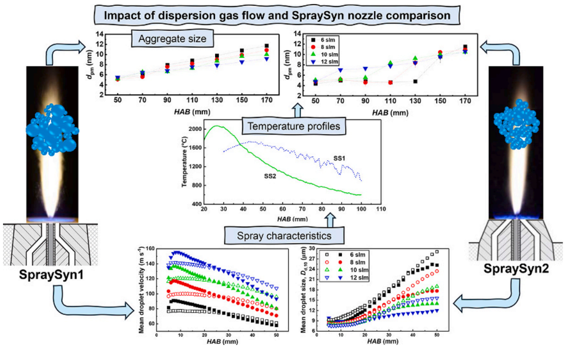

ARTICLE INFO

Keywords:
Spray flame synthesis
iron oxide nanoparticle
SpraySyn burner
Dispersion gas
Coaxial atomization
HiaT-SMPS

ABSTRACT

This study investigates the effect of dispersion gas (DG) flow on the formation and properties of maghemite (γ-Fe_2O_3) nanoparticles using standardized *SpraySyn* burners (SS1 and SS2). Several diagnostics were employed to characterize the spray and nanoparticles.

Increasing DG flow (6 – 12 slm) results in smaller droplet sizes (DS), cooler flame temperatures, shorter high-temperature droplet/particle residence times, and smaller agglomerates in the size range of 5 – 12 nm with narrower primary particle size distribution, corresponding to higher mass fractal dimensions, as supported by TEM and SMPS analysis, resulting in more compact agglomerates. BET and TEM confirmed decreasing primary

---

This article is part of a Special issue entitled: 'Gas-Phase Synth. Nanomat.' published in Powder Technology.

* Corresponding author.

E-mail address: hans-joachim.schmid@uni-paderborn.de (H.-J. Schmid).

https://doi.org/10.1016/j.powtec.2025.121992
Received 1 May 2025; Received in revised form 30 October 2025; Accepted 1 December 2025

particle sizes with increasing DG flow. Raman and XRD analyses predominantly identified maghemite, which shows a bimodal distribution of crystallite sizes, while SS1 samples have a greater proportion of larger crystallites.

The self-preserving size distributions of agglomerates with a geometric standard deviation of 1.5 are reached faster with increasing DG flow. The barrier effect of DG observed in SS1 leads to slower droplet combustion kinetics, higher temperatures, and delayed precursor release, which, along with downstream flow recirculation, result in significantly higher agglomeration rates outside the visible flame. SS2 demonstrates improved atomization, more stable flames, and finer, uniform nanoparticles with less carbonaceous residues (CR). Conversely, SS1 showed broader DS distributions and higher CR levels on the γ-Fe_2O_3 surface, especially at higher DG flow.

This work highlights the essential role of DG flow and nozzle geometry in controlling droplet evaporation, flame stability, and nanoparticle growth, offering insights for optimizing SFS and validating numerical models.

1. Introduction

Spray flame synthesis (SFS) is a scalable, efficient technique for producing high-purity nanomaterials. Compared with wet-phase synthesis, SFS offers advantages such as access to low-toxicity precursors, simplified processing, enhanced particle purity, and high crystallinity [1,2]. Nanomaterials produced using SFS are widely used in various applications, including catalysts, batteries, advanced pigments, gas sensors, biomaterials, bioimaging, biosensing, and nanotoxicology screening studies [2–9]. The key to SFS's success lies in its straightforward preparation process and the use of a combustible-liquid precursor solvent mixture, which allows the incorporation of nearly all elements from the periodic table in diverse combinations [10]. For instance, superparamagnetic maghemite (γ-Fe_2O_3) is widely used in biomedical applications such as drug delivery, hyperthermia, protein separation, and nanotoxicology research [7,8,11–14]. Maghemite production via SFS will be the focus of this study. It requires a combustible precursor solvent mixture—typically iron (III) nitrate nonahydrate (INN) as the precursor dissolved in ethanol (EtOH) and 2-ethylhexanoic acid (EHA)— which is atomized and ignited by a self-sustaining pilot flame, leading to nanoparticle formation via either a gas-to-particle or a droplet-to-particle pathway [1,15]. The gas-to-particle pathway is preferred for nanoscale material synthesis because it enables the formation of homogeneous, sub-10 nm aggregates (hard agglomerates) or agglomerates (soft agglomerates) in the gas phase, depending on the characteristic sintering or coagulation times [16]. In contrast, the droplet-to-particle route yields unwanted, large, hollow, shell-like aggregates with a broad particle size distribution. The droplet-to-particle pathway refers to particle formation in the liquid phase, characterized by precursor precipitation within the droplet or on its surface. The role of EHA in enhancing the chemical stability of the precursor solvent mixture against liquid phase reactions [17] and its impact on the gas-to-particle conversion have been confirmed by numerous studies of SFS and single-droplet combustion [15,18,19]. When using precursor solvent mixtures with high combustion enthalpies, such as EtOH and EHA, droplets undergo cascade-like microexplosions, which are associated with high powder quality. In addition, Jossen et al. [20] have formulated two criteria based on experimental investigations of numerous metal oxides. Homogeneous nanoparticles are formed at combustion enthalpy densities greater than 4.7 kJ/g_{gas} and when the ratio of the solvent boiling point to the melting or decomposition point of the metal precursor is greater than 1.05. Moreover, for well-defined nanomaterial characteristics, it is important to tailor the SFS process by controlling certain key process parameters, such as the flow rates of precursor solvent, dispersion gas, and co-flow, as well as the precursor concentration and solvent composition [21–24]. To compare results across laboratories, a standardized burner design is essential. In response to this need, Schneider et al. [25] introduced the *SpraySyn* 1.0 burner (SS1), which has been extensively studied within the German priority program SSP1980 [26] to gain a comprehensive understanding of the entire nanoparticle synthesis process. Several numerical [27–34] and experimental [24,30,35–41] studies have investigated the fundamentals of iron oxide formed via SFS. Some characteristics of SS1 have been identified in these studies. In addition, Bieber et al. [35], Karaminejad et al. [30], and Kumar et al. [42] have shown that SS1 flames exhibit millisecond-range pulsations due to an aperiodic atomization process. Lang et al. [43] recently showed this for SS2. This flame instability arises primarily from the parallel alignment of the capillary and dispersion gas streams, which creates a barrier between the pilot flame and the atomized liquid precursor solvent. Such flame pulsations result in significant temporal and spatial fluctuations in particle synthesis within the spray flame. An angled dispersion gas line was introduced to address this issue. This results in increased flame activity over time and improved atomization due to significantly greater average radial momentum transfer, shear, and turbulence. It facilitates interaction between smaller droplets and the pilot flame [35]. The design of a new *SpraySyn* burner (SS2) with this key feature was implemented and subjected to manifold works. SS2 provides finer nanoparticles with a higher specific surface area and less residual content in the product [35,44]. Tischendorf et al. [35,45] have examined the evolution of agglomerates along the flame centerline by measuring the number-weighted mean electrical mobility diameter at identical operating conditions using in-situ scanning mobility particle sizing. They found an atypical agglomerate dynamic within the SS1 flame, characterized by a significant increase in the agglomeration rate outside the visible flame. The present study explores the relationship between the dispersion gas (DG) flow and particle evolution previously observed in SS1. Additionally, a similar investigation is conducted in SS2. The study compares the droplet and powder characteristics produced by both *SpraySyn* burners. This research can be crucial for validating simulations, as such data are still lacking in the literature for the standardized *SpraySyn* burners. Adjusting the DG flow rate controls the turbulent mixing zone, primary particle growth, cold air entrainment from the surroundings, and subsequent recirculation. The high-temperature particle residence time (HTPRT) is greatly influenced by DG flow, as demonstrated by Gröhn et al. [46] in their study of the zirconia (ZrO_2) nanoparticle produced through SFS. Other authors have studied the effects of spray parameters (DG and precursor solvent flow rate) on the nanoparticle synthesis of ZrO_2 [10,47], wolfram (WO_3) [48], and iron oxide (γ-Fe_2O_3 and Fe_3O_4) [49] using different burner geometries.

2. Materials and methods

2.1. Iron oxide synthesis and experimental setup

In this study, iron oxide nanoparticles were synthesized using iron (III) nitrate nonahydrate ($Fe(NO_3)_3 \cdot 9H_2O$, 98 % purity, Thermo Fischer Scientific GmbH) as the precursor source, dissolved at a concentration of 0.1 mol l^{-1} in a solvent mixture of ethanol (99.8 % purity, Th. Geyer GmbH & *Co.* KG), and 2-ethylhexanoic acid (99 % purity, Thermo Fischer Scientific GmbH) in a 35:65 vol% ratio. The total water content in the mixture (including the solvent and precursor) was 1.83 wt%. The solution was stirred for 30 min at room temperature prior to synthesis, and all chemicals were used without further purification. The synthesis was operated in an open-flame configuration. The standardized burners (SS1 and SS2, respectively), developed within the priority project mentioned above, have been described in detail elsewhere [25,35]. The SFS process is described in Fig. 1. The liquid precursor solvent was supplied at 2 ml min^{-1} via a syringe pump (KDS Gemini 88 Plus, KD Scientific Inc.) through a capillary (1) and atomized using oxygen (O_2, 99.5 % purity) as dispersion gas (2). The resulting droplets were ignited in a coaxial premixed diffusion flame (annular pilot flame, 2 l min^{-1} CH_4, and 16 l min^{-1} O_2) stabilized by a bronze matrix (3). Assuming stoichiometric CH_4 combustion in the pilot flame (PF), an oxygen excess of 75 % ($\phi = 0.25$) was achieved. All gas flows were controlled using calibrated mass flow controllers (Bronkhorst High-Tech B.V.) under standard conditions ($T = 0$ °C and pressure $p = 1.01325$ bar). Subsequently, nanoparticle formation occurred within the highly reactive, turbulent spray flame via nucleation, agglomeration/aggregation, sintering, and surface growth, ultimately yielding fractal-like nanoparticles. A co-flow of 120 l min^{-1} filtered air (4) was used to stabilize the flame and ensure reproducibility. The synthesized aerosol was extracted through a fume hood at 220 mm height above the burner (HAB) using a vacuum pump (Mink MM 1144 BV, Dr.-Ing. K. Busch GmbH) operating at 60 m^3 h^{-1}. The aerosol travelled 1 m through a DN40 tube, with a residence time of 75 ms before being collected on a surface filter (ePTFE membrane, R + B Filter GmbH). During transport, the aerosol cooled to 150 °C [45], preventing the alteration of particle properties on the filter due to excessive heat. Because the phase transformations and sintering of iron oxide agglomerates occur at higher temperatures, the aerosol temperature at the nanoparticle collection position was suitable for the experiments. The maghemite-to-hematite (α-Fe_2O_3) crystal phase transformation occurs at temperatures >300 °C [49–51], whereas iron hydroxides, potentially formed via the droplet-to-particle pathway, transform at temperatures in the range of 200 – 300 °C [49,52].

2.2. Spray characterization

Droplet velocity and size measurements were performed using Phase-Doppler Anemometry (PDA). To characterize the spray atomization behavior in the active flame context, the spray flame was scanned along the axial direction from 5 mm to 50 mm HAB. The combustion chamber was mounted on three linear translation stages for precise alignment and repeatability, allowing movement in the x, y, and z directions with a minimum increment of 0.1 mm. This scanning approach ensured coverage of the spray flame region, enabling droplet size characterization across different flame regions. A dual-wavelength laser source (ILA 2D fp50 LDV System, 250 mW at 532 nm and 561 nm) provided the incident beams. A DANTEC PDA Classic receiver, equipped with a BSA P80 processor, detected the scattered light and processed the droplet signals. The receiver was positioned at a scattering angle of 65° to minimize the influence of refractive index variations in the flame, which can arise due to localized evaporation of more volatile components in the solvent mixture [53].

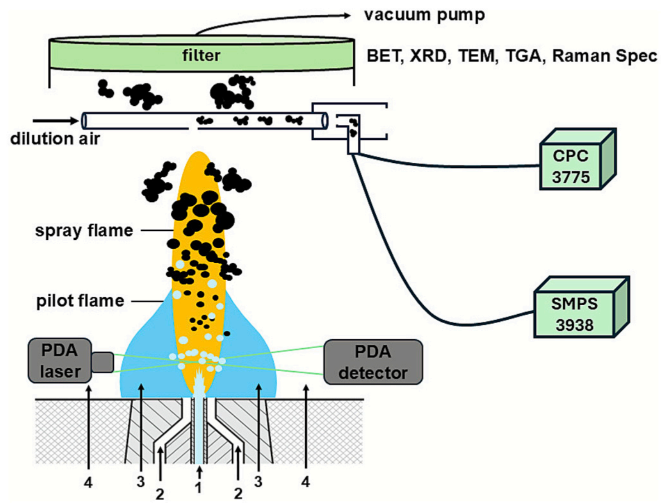

Fig. 1. Experimental setup for particle synthesis using the SS1 burner and experimental evaluation. With volumetric inlet flows of the liquid solvent precursor (1), oxygen dispersion gas (2), premixed methane/oxygen for the pilot flame (3), and air co-flow (4).

2.3. Flame and gas characterization

Spectral-narrow-band imaging of flame radicals is a well-established diagnostic technique for analyzing reactive flows, as it enables selective visualization of specific intermediate species and their corresponding reaction zones [54–56]. In the present study, spectrally narrow-band imaging of spontaneous OH* and CH* radical emissions was performed to visualize the flame structure and identify reaction zones. The experimental setup consisted of a LaVision FlowMaster 3 camera coupled to a LaVision Image Intensifier IRO, positioned to image the central cross-section of the burner through an F-mount UV camera objective. To achieve high spatial resolution, the CCD camera was configured to capture 170 images at a rate of 2 frames per second, yielding a pixel resolution of approximately 0.05 mm/pixel. Bandpass filters with a 10 nm bandwidth were placed in front of the intensifier: one centered at 308 nm for OH* (transmissivity of 15 %) and another centered at 430 nm for CH* (transmissivity of 45 %).

Although these filters primarily isolate the spectral emission peaks for OH* and CH*, they can also transmit portions of broadband radiation from soot particles or CO_2 [57].

Despite this potential background emission, band-pass filters remain a valuable method for identifying different phases of the combustion process. OH* imaging highlights areas of strong heat release, while CH* identifies the primary flame front. In this study, the normalized narrow-band images were used qualitatively, focusing on the location and shape of the reaction zones rather than on absolute intensity measurements. As a result, the technique provided critical insight into the spatial distribution of key intermediates in the flame, offering an understanding of the underlying chemical and thermal structures governing the spray flame synthesis.

A z-type Schlieren system was employed to visualize the gas flow and density variations in the spray flame synthesis [58]. A high-speed incoherent diode laser (Cavitar Cavilux Smart, wavelength of 640 nm) served as the illumination source, providing a sufficiently bright and stable beam for high-speed imaging. Two parabolic mirrors, each with a diameter of 203.2 mm, were arranged in the characteristic z-configuration: the first mirror collimated the laser beam across the test section, and the second mirror refocused it onto a knife-edge cutoff. This setup produced high-contrast Schlieren images by selectively blocking or passing refracted rays, thereby revealing refractive index gradients in the flow. The resulting schlieren patterns were recorded with a Photron Nova S12 high-speed camera at 10,000 frames per second, capturing rapid flow structures and transients. While this method provides a visual tool for assessing density gradients and flow phenomena, it does not directly measure density. Instead, schlieren imaging principally offers a qualitative representation of where and how strong density variations occur. Nonetheless, this approach is beneficial for observing the influence of the dispersion gas flow on the spray flame process, as it clearly highlights the mixing zones and the dynamic interactions governing the development and stability of the flame. From the Schlieren images, the position of the strongest entrainment relative to the burner was obtained.

2.4. Agglomerate characterization

The size distribution of aggregates/agglomerates extracted using a sampling probe called a hole-in-a-tube (HiaT) was measured using a scanning mobility particle sizer (SMPS). HiaT-SMPS was used in recent publications to investigate particle evolution in SFS. Goudeli et al. [59], and Gröhn et al. [60] have used HiaT-SMPS to characterize the evolution of zirconia nanoparticles made by SFS. Tischendorf et al. [44,45] have studied the relevance of successive quenching experiments to get reliable HiaT-SMPS data. These experiments consist of stepwise sample dilution until the mean electrical mobility diameter shows no further change with increasing dilution flow rate, i.e., the aerosol is assumed to correspond to the real aerosol in the flame. As a result, particle agglomeration during the transport is sufficiently reduced.

The extracted sample is diluted using particle-free dry air flow, as shown in Fig. 1. At the sampling tube outlet, the diluted aerosol flow expands into an open plastic tube where two streams are sucked. The condensation particle counter (CPC, type 3775, TSI Inc.) measures the current total aerosol number concentration with a cut-off size of 4 nm, operating at a flow rate of 0.3 $\mathrm{l\ min^{-1}}$. The CPC device is a significant indicator of the quenching level during measurements. The SMPS™ (model 3938, TSI Inc.) operated in the range of $1-30$ nm and consisted of a classifier 3082, an X-ray neutralizer 3088, a differential mobility analyzer (DMA) type 3086, a nano-enhancer 3757 using diethylene glycol as fluid, and a butanol-based CPC type 3750. It was operated at negative polarity, with a sheath flow of 25 $\mathrm{l\ min^{-1}}$, and aerosol flow of 2.5 $\mathrm{l\ min^{-1}}$ passing through the nano-enhancer. The measurement settings were similar to those used by Tischendorf et al. [44,45]. The scans were performed at the CPC number concentration range of $\sim 7\times10^4 - 2\times10^5\#\mathrm{cm^{-3}}$, with a scan time of 180 s. The reproducibility of the measurements was assessed by performing three scans at each HAB. The average values with 95 % confidence intervals are evaluated and discussed in Section 3.

2.5. Analytical burner parameters and flame structure

The process conditions in the flame — namely, droplet generation, flow, chemical reactions, and particle formation — are governed by several dimensionless characteristic numbers. Therefore, the following global parameters were determined independently of the burner geometry based on the chemical reactions in the spray, including precursor decomposition, and in the pilot flame. The equivalence ratio, ϕ, is the ratio of the oxygen flow rate required for stochiometric hydrocarbon combustion to the experimentally provided oxygen flow rate to the burner. ϕ is calculated with Eq. (1) assuming all process gas flows (i.e., flows 1–3 in Fig. 1) containing oxygen contribute equally to the total oxygen (O_2) supply.

$$\phi = \frac{\dot{n}_{O_2,stoic}}{\dot{n}_{O_2,exp}} \tag{1}$$

O_2 originating from the ambient environment, and the co-flow is neglected. The combustion enthalpy density referred to the dispersion gas

$$\Delta_R H_{gas} = -\frac{\dot{n}_{precursor}\Delta_R H_{precursor} + \dot{n}_{solvent}\Delta_R H_{solvent} + \dot{n}_{CH_4}\Delta_R H_{CH_4}}{\dot{m}_{O_2,DG}} \tag{2}$$

and

$$\Delta_R H_{tot} = -\frac{\dot{n}_{precursor}\Delta_R H_{precursor} + \dot{n}_{solvent}\Delta_R H_{solvent} + \dot{n}_{CH_4}\Delta_R H_{CH_4}}{\dot{m}_{O_2,DG} + \dot{m}_{precursor+solvent} + \dot{m}_{CH_4,PF} + \dot{m}_{O_2,PF}} \tag{3}$$

to all inlet mass streams is calculated according to [20,61], respectively. $\Delta_R H$, $\dot{n}$ and $\dot{m}$ represent combustion enthalpy calculated with standard combustion enthalpies at 25 °C, mol flow, and mass flow rate, respectively.

Table 1 lists some burner parameters calculated for all process conditions. The power supply to the burner, due to hydrocarbon combustion, is 1.95 kW. The pilot flame accounts for 61 % of the total power.

The following key dimensionless numbers are known to describe the atomization conditions resulting from the parameter variations: jet Reynolds numbers for the gas and liquid phases (Re_g and Re_l), aerodynamic Weber number (We_{aero}), momentum flux ratio between gas and liquid (M), gas-to-liquid mass ratio GLMR, and Mach number Ma (Table 2). The dimensionless numbers are intended to provide a comprehensive overview of the spray-flame boundary conditions at the nozzle outlet. However, no correlation based on the dimensionless numbers is intended to be derived here.

Table 1
Analytical burner parameters calculated for all process conditions. The mentioned power refers to the total power theoretically provided by the pilot and spray flame.

DG (slm)	power (kW)	$\Delta_R H_{gas}$ (kJ g^{-1})	$\Delta_R H_{tot}$ (kJ g^{-1})	ϕ (−)
6	1.95	13.68	3.38	0.31
8	1.95	10.26	3.13	0.28
10	1.95	8.21	2.90	0.26
12	1.95	6.84	2.71	0.24

$$Re_g = \frac{u_g \rho_g d_h}{\eta_g} \tag{4}$$

$$Re_l = \frac{u_l \rho_l d_c}{\eta_l} \tag{5}$$

$$We_{aero} = \frac{(u_g - u_l)^2 \rho_g d_c}{\sigma_l} \tag{6}$$

$$GLMR = \frac{\dot{m}_g}{\dot{m}_l} \tag{7}$$

$$\mathrm{M} = \frac{u_g^2 \rho_g}{u_l^2 \rho_l} \tag{8}$$

$$\mathrm{Ma} = \frac{u_g}{c} \tag{9}$$

$\rho_{g/l}$ and $\eta_{g/l}$ describe the density and viscosity of DG and precursor solvent, respectively. DG density is calculated assuming the ideal gas law at atmospheric pressure and room temperature, and viscosity was taken from [62]. The precursor solvent properties have been measured and reported in [24]. $d_{h/c}$ represents the hydraulic diameter (0.7 mm) of the dispersion gas inlet and the diameter of the precursor solvent capillary (0.4 mm), respectively. $u_{g/l}$ and $\dot{m}_{g/c}$ are exit velocity and mass flow rate of gas and precursor solvent. $c = 343\ \mathrm{m\ s^{-1}}$ represents the speed of sound of dry air at 20 °C [62].

2.6. Powder characterization

To characterize the final powder properties, particles were collected on the filter downstream of the SFS. These samples were characterized by a number of complementary measurement methods.

2.6.1. Thermogravimetric analysis of samples (TGA-DSC-MS)

Due to different droplet/temperature histories and residence times within the spray flame, the possibility of incomplete droplet evaporation remains significant, potentially leading to incomplete precursor conversion in the flame. Therefore, solvent, nitrate-based residues, and carbonaceous by-products deposited on particle surfaces during the SFS [40,44] were investigated by performing thermogravimetric analysis (TGA) and differential scanning calorimetry (DSC), coupled with mass spectrometry (MS; QMS 403 Aëolos quadrupole mass spectrometer) to monitor the gas phase environment. The TGA-DSC analysis was conducted using a STA 449 F1 Jupiter device. The samples ($11-40$ mg) were pressed into pellets and subjected to a temperature range of $25-900$ °C in a silicon carbide furnace under air atmosphere, with a heating rate of 10 °C $\mathrm{min^{-1}}$. The MS tracks the mass-to-charge (m/z) ratios of 18

Table 2
Operating conditions of the burners and corresponding dimensionless values at nozzle exit. Δp corresponds to the static pressure drop of the dispersion gas flow.

DG (slm)	u_g (m/s)	Re_g (−)	Re_l (−)	We_g (−)	Ma (−)	M (−)	GLMR (−)	Δp_{SS1} (bar)	Δp_{SS2} (bar)
6	77.6	4076.5	20.5	120.9	0.23	126.2	4.7	0.10	0.48
8	103.5	5435.4	20.5	215.2	0.30	224.4	6.3	0.18	0.59
10	129.4	6794.2	20.5	336.6	0.38	350.5	7.9	0.22	0.75
12	155.2	8153.0	20.5	485.1	0.45	504.8	9.5	0.32	0.89

(H_2O), 44 (CO_2), and 30 (NO_x), which help to determine the nature of the residues in the samples.

2.6.2. *The specific surface area (SSA)*

Brunauer-Emmett-Teller (BET) N_2- physisorption provides insights into the specific surface area (*SSA*) [63]. The *SSA* of iron oxides was measured using a Quantachrome Autosorb 6 at −196 °C after degassing the samples under vacuum at 120 °C overnight. The calculation utilized five data points within the relative pressure range of $0.1-0.3$ according to [64]. Based on *SSA*, the average primary particle size $d_{p32,BET}$ of the powder is calculated assuming spherical particles:

$$d_{p32,BET} = 6/\left(\rho_p \cdot \mathrm{SSA}\right) \tag{10}$$

where $\rho_p = 4.88\ \mathrm{g\ cm^{-3}}$ [65], represents the γ-Fe_2O_3 density.

2.6.3. *Transmission electron microscopy (TEM/HRTEM)*

TEM/HRTEM analysis of the samples was carried out on a JEOL JEM-ARM200F high-resolution microscope (Cs-correction, field emission HRTEM-STEM) to investigate the particle morphology and crystallinity and to estimate the primary particle size. The samples were dispersed in isopropanol (Th. Geyer GmbH & *Co*. KG), using ultrasonication (BANDELIN Electronic, type DK 510-P) for 20 min. Then, some drops of the suspension were placed on conventional carbon-coated Cu-grids (S160, PLANO GmbH). The primary particle sizes are determined manually using image processing in ImageJ (Wayne Rasband, [66]). To compare primary particle size from HR-TEM with $d_{p32,BET}$, the Sauter mean diameter $d_{p32,TEM}$ [67] is derived from the number-based primary particle size distribution (PPSD) obtained from image processing by the following equation:

$$d_{p32,TEM} = \frac{\sum_{i=1}^{i_{max}} \left(n_i \cdot d_{p,TEM}^3\right)}{\sum_{i=1}^{i_{max}} \left(n_i \cdot d_{p,TEM}^2\right)} \tag{11}$$

With n_i representing the counts of primary particles in each bin of size $d_{p,TEM}$.

2.6.4. *Raman spectroscopy*

The crystalline phase is identified by Raman spectroscopy. The analysis was conducted using a confocal Raman microscope (Renishaw plc., model inVia Re04). A low laser power of 0.15 mW at a laser wavelength of 633 nm was used to prevent the possible transformation of metastable maghemite into stable rhombic paramagnetic hematite phase.

2.6.5. *X-ray diffraction (XRD)*

XRD analysis was conducted as a complementary technique to the Raman spectroscopy to identify and characterize crystalline phases and their respective crystallite sizes. Measurements were performed using a Rigaku Smartlab diffractometer equipped with a Cu K-alpha radiation source ($\lambda = 1.5406$ Å), operating at 45 kV and 200 mA in Bragg-Brentano geometry. Diffraction patterns were collected over a 2θ range of $10-80^\circ$ with a step size of 0.06° and a scan rate of $3^\circ\ \mathrm{min}^{-1}$. To minimize background scattering, the samples were prepared on a silicon single crystal (911) sample holder. The resulting diffractograms were subjected to Rietveld analysis to quantify crystalline phases and their respective crystallite sizes using the MAUD software package (rev. 29,993). To account for instrumental contributions to peak broadening, a correction was applied based on measurements of a LaB_6 reference powder (NIST SRM 660) under identical measurement conditions. This correction was implemented across all analyses in this study.

3. Results and discussion

3.1. *Spray characteristics*

Fig. 2 depicts droplet characteristics measured along the spray flame centerline by PDA in dependence on HAB for both burners. The curves for mean droplet velocity in Fig. 2a and mean droplet size in Fig. 2b exhibit a similar trend for both burners, showing reduced droplet sizes and increased droplet velocities with increasing dispersion gas flows (increasing GLMR). The reduction in droplet size with increasing GLMR (or increasing Weber and jet Reynolds numbers) is in line with expectations. The mean droplet diameter D_{d10} along the flame centerline initially decreases with respect to HAB for both burner types, reaching a minimum at around 10 mm HAB. The decline of D_{d10} is due to a combination of fast evaporation of small droplets (radius-square-law) and secondary atomization. This effect of small droplet evaporation is particularly emphasized, as the arithmetic mean droplet diameter is displayed. Beyond the minimum, D_{d10} increases with HAB, since the evaporation of small droplets is completed, and solely relatively large droplets are left to be detected by PDA [24]. Fig. 2c and d clearly indicate the complete evaporation of small droplets with increasing HAB, while only large droplets are still present further downstream. At 50 mm HAB, only 18,217 and 1768 droplets (for SS1 and SS2, respectively) were detected, compared to the 50,000 droplets measured at 20 mm HAB for both burners. The droplets are accelerated during this significant evaporation regime until ∼ 8 mm HAB; afterwards, the mean droplet velocity decreases due to air entrainment, increasing flow cross-section, friction, dissipation, and gravitational forces [35,37]. This droplet acceleration is more pronounced for SS2, indicating higher average velocity in the considered HAB range and shorter high-temperature droplet residence time [35]. Considering the SS1 burner, D_{d10} initially decreases slightly from a starting range of approximately $8-9$ μm at low HAB < 10 mm across all DG flow rates. After this initial decrease, D_{d10} increases sharply with further HAB. This increase is more significant with decreasing dispersion gas flows. For 6 slm, D_{d10} rises steeply from about 9 to 28 μm, while for 12 slm D_{d10} increases slightly up to 16 μm at 50 mm HAB. In comparison, the initial decrease in D_{d10} is more pronounced in SS2, followed by a considerably smaller increase with HAB than in SS1. At HAB < 10 mm, mean droplet sizes range from 6 to 9 μm, similar to SS1. Beyond this range, D_{d10} rises from 9 to 25 μm and only up to 12 μm, at 6 and 12 slm, respectively.

The SS1 burner shows greater atomization sensitivity to increased dispersion gas flow rates, with significant differences in mean droplet size between 6 and 12 slm. In contrast, SS2 produces smaller droplets across all flow conditions, indicating a more efficient atomization. The increase in the mean droplet size in SS1 with HAB suggests incomplete droplet evaporation. A possible droplet coalescence is excluded since the droplet concentration continuously decreases with HAB due to evaporation and dilution by external gas. In addition, droplet-droplet in-

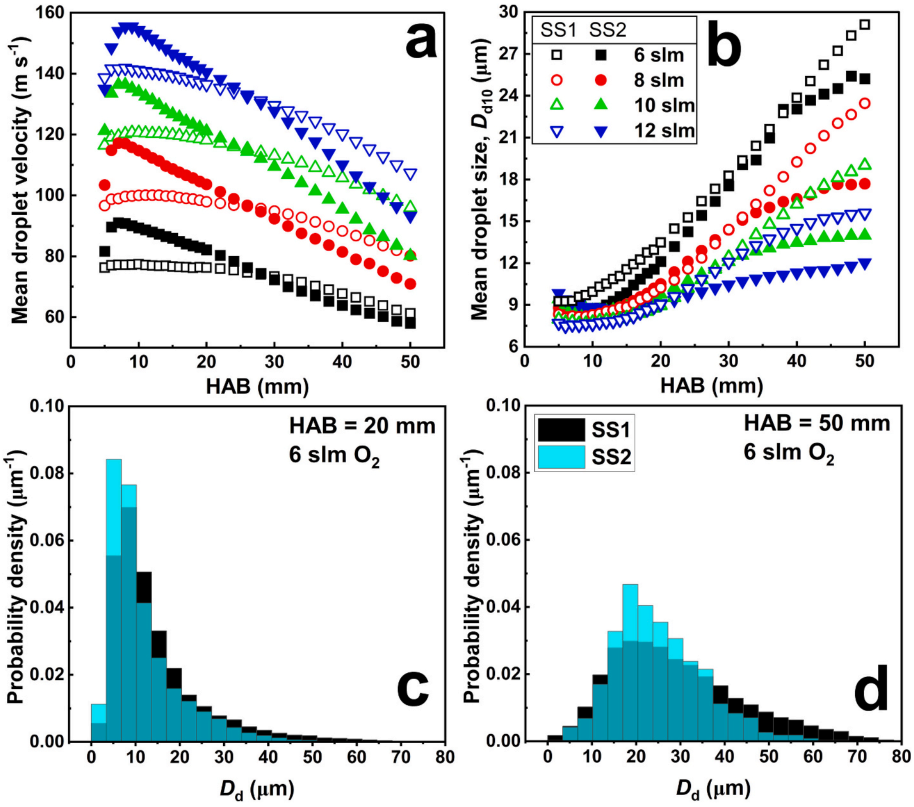

Fig. 2. (a) Axial mean droplet velocity profiles; (b) corresponding arithmetic mean droplet diameter D_{d10} profile for both burners at varying dispersion gas flow rates (open symbols correspond to SS1 and solid to SS2); (c, d) number-based probability density histograms of the droplet size distribution for 6 slm measured by PDA at 20 and 50 mm HAB [68].

teractions are negligible at droplet concentrations lower than $\sim 3 \times 10^4 \#\text{cm}^{-3}$ [69].

3.2. Temperature profiles

Fig. 3a shows the flame temperature profile along the spray flame centerline, measured by a type R thermocouple (250 μm) for two dispersion gas flows of 10 and 12 slm. The effect of radiation on the reported temperature values is corrected according to [70]. Note that temperature measurements for SS1 could not be performed at HAB < 30 mm because the thermocouple was damaged by droplet decomposition and subsequent reactions on its surface. The temperature profiles of SS1 and SS2 reveal distinct thermal characteristics. Considering SS1, at 30 mm HAB, the spray flame temperature is 1519 and 1451 °C for 10 and 12 slm, respectively. This corresponds to a temperature drop of $\Delta T = 68$ °C with increasing DG flow. The temperature increases steadily to a peak of 1718 and 1600 °C at ~50 mm HAB, then drops to 898 and 839 °C at 100 mm HAB. However, SS1 exhibits significant temperature fluctuations at higher HAB, indicating unstable droplet ignition and combustion dynamics. As previously mentioned, flame pulsations observed in SS1 result in substantial temporal and spatial changes of spray flame conditions, which influence particle properties. Moreover, increasing the dispersion gas flow at constant precursor solvent flow reduces the flame stability [71,72].

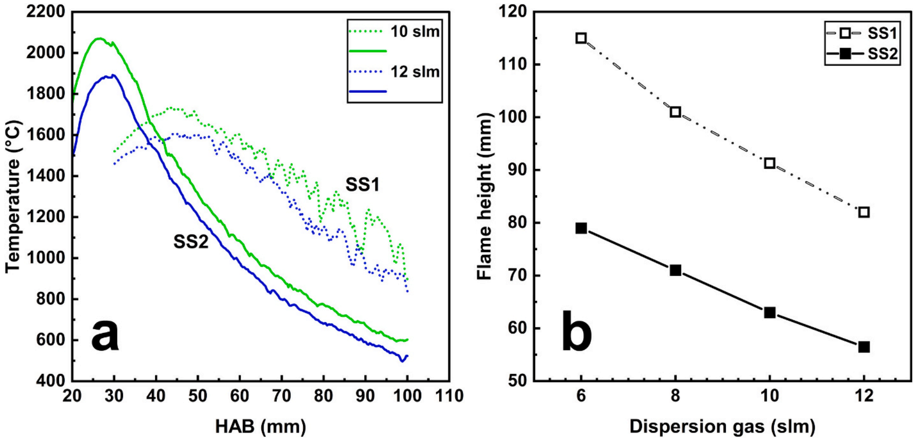

Fig. 3. (a) Temperature profiles of SS1 and SS2 as a function of HAB for dispersion gas flow rates of 10 and 12 slm, determined by thermocouple, and (b) visible flame height across all dispersion gas flows investigated in this study.

In contrast, the SS2 temperature profiles exhibit higher peaks for both DG flows considered in Fig. 3a at around 2070 and 1884 °C, respectively. The temperature peaks are reached earlier at ∼27 mm HAB with $\Delta T = 186$ °C, followed by a steady, gradual, and steep decrease in temperature. The pronounced temperature drop suggests a faster cooling rate in SS2. The reduction in flame temperature at higher DG flow rates is primarily due to the increased volume of gas and cold air entrainment from the open surrounding that must be heated at constant remaining combustion enthalpy supply, leading to reduced visible flame height (see Fig. 3b). Interestingly, the position of local maxima of the temperature profile (12 slm, SS2 burner) correlate well with the high CH*/OH* emissions at around 30 mm HAB Fig. 4, where quenching dominates. Gröhn et al. [46] have determined the cumulative air entrainment as a function of HAB for the SFS of ZrO_2, showing an approximately linear increase with HAB. A higher DG flow rate at a constant precursor feed rate results in a higher initial momentum flux (see Table 2), thereby increasing overall cold air entrainment. Furthermore, this increase in cold air entrainment is influenced by reduced temperature and lower volumetric gas expansion [73,74]. The colder spray flame observed at higher flow rates directly affects particle formation, size, and morphology, as well as the tendency toward aggregation or agglomeration, as shown later.

3.3. *Schlieren and chemiluminescence analysis*

Temporally averaged, spectrally narrow-band images of CH* and OH* emissions, combined with Schlieren images of the spray flame, are shown in Fig. 4 for dispersion gas flows of 6 and 12 slm for the SS2 burner. In lean flames, increasing the dispersion gas flow rate decreases the overall heat release region, as indicated by the OH* emission zone. This behavior is consistent with the expected reduction in flame temperature due to increased dilution and a reduced fuel-to-oxygen ratio per unit volume. From the CH* emission images, a shift in the emission toward higher HAB is observed at higher dispersion flow rates and, hence, higher fuel velocity, indicating the influence of the flow field on the flame shape. The Schlieren images also show stronger entrainment closer to the burner at a higher dispersion gas flow. The entrainment point moves down to about 21 mm HAB at 12 slm from 27 mm HAB at 6 slm.

3.4. *Agglomerate characteristics*

The results of the HiaT-SMPS measurements at the flame centerline are presented in this section. The corresponding particle size distributions in dependency of HAB are displayed in the Supplementary materials in Fig. S1 and S2. Fig. 5a and c illustrate the evolution of the agglomerates' average mean electrical mobility diameter ($\overline{d}_{\mathrm{pm}}$) for SS1 and SS2, respectively. Fig. 5b and d show the corresponding number-based geometric standard deviations $\sigma_{\mathrm{gn,SMPS}}$. The impact of nozzle geometry is emphasized in Fig. 6a and b, where $\overline{d}_{\mathrm{pm}}$ and $\sigma_{\mathrm{gn,SMPS}}$ are plotted for each DG flow. Regarding the agglomerate dynamic in the SS1 burner, a systematic jump in $\overline{d}_{\mathrm{pm}}$ at the flame tip is observed for each DG flow (cf. Fig. 5.a). This abrupt jump occurs earlier as the dispersion gas flow rises. No significant growth in size is measured before this jump. At 6 slm, the agglomeration is minimal from 5 to 130 mm HAB (from 4.35 nm to 4.83 nm, reflecting an increase of 0.5 nm). However, between 130 and 150 mm HAB, a sudden growth in size occurs, reaching 9.64 nm. Afterwards, only a moderate increase in mobility diameter occurs ($\overline{d}_{\mathrm{pm}} = 11.54$ nm). At 12 slm, this abrupt agglomeration occurs earlier at HAB $= 50$ mm. The $\overline{d}_{\mathrm{pm}}$ increases from 4.90 to 7.03 nm. Beyond this point, a linear increase in $\overline{d}_{\mathrm{pm}}$ is observed, culminating in a final value of 10.58 nm. Despite the sudden pronounced agglomeration observed for each DG flow rate, the expected influence of DG on particle size at constant HAB becomes apparent only beyond 150 mm HAB, where a slight decrease in size with increasing DG flow is noted. The particle size distributions (PSD) at the locations directly after the jumps in $\overline{d}_{\mathrm{pm}}$ are plotted in Fig. 7. As DG flow increases, $\sigma_{\mathrm{gn,SMPS}}$ decreases (1.64, 1.79, 1.49, and 1.47). The PSDs are normalized to the modal values, as the exact dilution ratio (defined as the dilution flow to aerosol flow ratio) of the extracted aerosol remains unknown, preventing the determination of absolute number concentration. Multimodal, bimodal, and monomodal distributions are observed, indicating a reduction in agglomerate polydispersity. This might be explained as follows: (i) The barrier effect of the coaxial dispersion gas flow observed in SS1 leads to the exit of droplets from the high-temperature region, resulting in prolonged droplet lifetime and late evaporation. Thus, late particle formation — most likely through nucleation or potentially through droplet-to-particle conversion — occurs even at lower sintering rates due to irregular local heat distribution. The former reduces the average primary particle size and broadens the particle (agglomerate) size distribution, while the latter produces larger nanoscale particles. Agglomeration prevails significantly further downstream. At higher DG flow, the polydisperse characteristic of agglomerates is suppressed, since small droplets evaporate faster, and particle formation and agglomeration occur earlier. (ii) The infiltration of cold air from the surroundings increases with increasing DG flow. This effect is associated with flow recirculation within the gas jet. This might be accompanied by particles around the flame tip, close to the centerline, that have experienced significantly

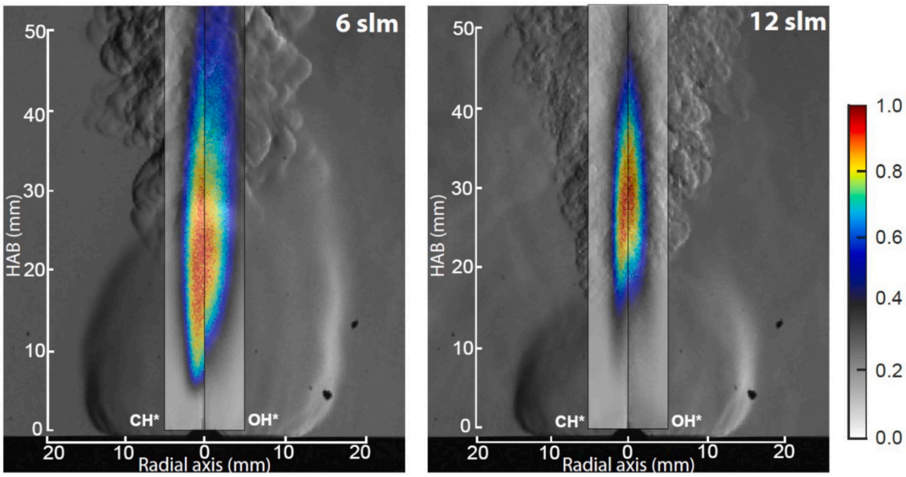

Fig. 4. Schlieren images of solvent mixture flames for the SS2 burner with two different O_2 dispersion flow rates: 6 slm (left), and 12 slm (right). Normalized CH* (left half) and OH* (right half) emission images are placed on the Schlieren images for better visual representation of the flames [68].

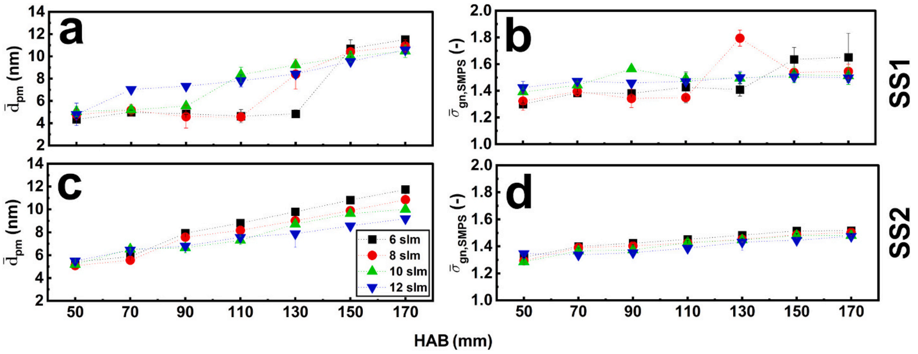

Fig. 5. Agglomerate average mean mobility diameter as a function of dispersion gas and (b, d) the corresponding number-based geometric standard deviation (with 95 % confidence interval) measured by HiaT-SMPS during synthesis with SS1 and SS2 burners.

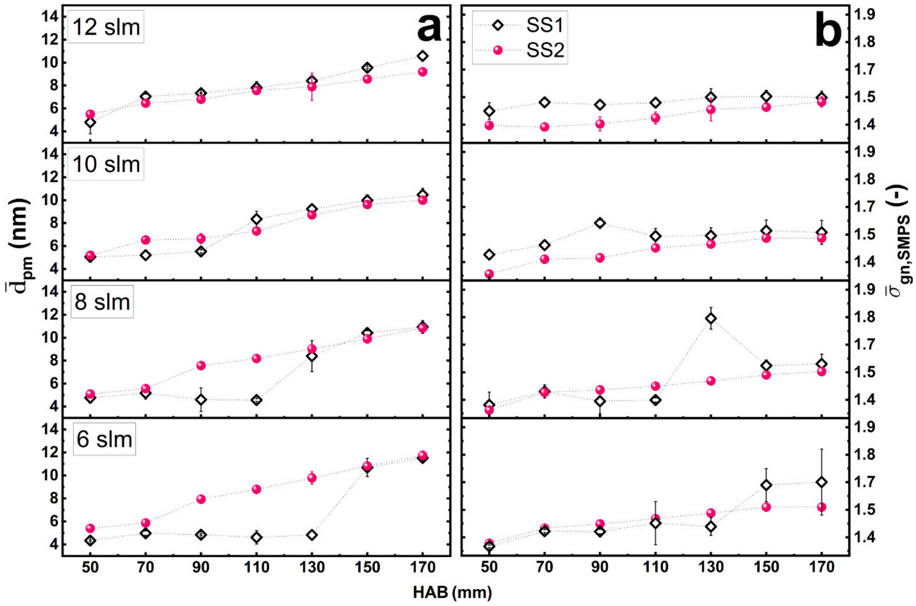

Fig. 6. Agglomerate average mean mobility diameter and the corresponding number-based geometric standard deviation plotted separately for each dispersion gas flow to exhibit the nozzle geometry impact.

longer residence times and show a higher degree of agglomeration.

The dynamic of agglomerates observed by SS1 aligns with the findings of Heine et al. [69], who modeled the formation and growth of ZrO$_2$. One main insight from this study is the overlap between particle formation and evaporation of monodisperse 10 – 40 μm droplets. The explanation (i) provided here is also supported by this study [69]. In addition, the geometric standard deviation of particles converges toward the self-preserving limit (1.514) under high droplet combustion kinetics according to Heine et al. A similar trend is also seen in Fig. 5d for SS2, where fast droplet evaporation is observed. The agglomeration shown in Fig. 5c for SS2 follows a systematic trend across different DG flow rates. At HAB = 50 mm, the initial mobility particle diameter is ∼4 – 5 nm and increases linearly thereafter with HAB. This linear trend is a typical growth by coagulating agglomerates with short particle residence time in the hot flame zone [16]. A consistent influence of DG flow on $\bar{d}_{pm}$ is observed at each HAB, with reduced agglomerates at higher DG flow, corresponding to reduced residence time.

3.5. Powder characteristics

3.5.1. TGA-DSC-MS

The relative mass losses (i.e., adsorbed gases and powder impurities) of the samples produced by both burners during their thermal treatment are highlighted in Fig. 8a. All samples exhibit qualitatively similar thermal behavior. Each sample experiences a noticeable mass loss in the temperature range up to 300 °C, which can be attributed to the release of nitrogen oxides, CO$_2$ and water as indicated by mass spectrometric (MS) analysis (see Fig. 9). The initial release of NO$_x$ is followed by the release of CO$_2$ and water starting at around 175 °C [75–77], which is accompanied by a strongly exothermic signal observed in the DSC measurements. The NO$_x$ release is related to adsorbed nitric acid (HNO$_3$) formed during the decomposition of iron nitrate [78]. The presence of residual iron nitrate could also be considered. In this case, an endothermic DSC signal would be expected. However, this was not observed. This is attributed to the fact that, compared with the MS signals for CO$_2$ and H$_2$O, those for NO$_x$ are significantly weaker (approximately two orders of magnitude), especially for samples from SS2. These signals may be obscured by background noise. Moreover, intermediate oxidation processes of adsorbed hydrocarbons with NO$_x$ cannot be excluded. Their exothermic reaction with the oxygen in the surrounding atmosphere to form water and CO$_2$ results in a strongly exothermic DSC signal and is associated with oxidation of adsorbed carbonaceous byproducts formed during the SFS. These carbonaceous byproducts were identified through ATR-FTIR analysis as surface-bound carboxylates (R-CO$_2^-$) and carbonates (CO$_3^{-2}$) [44,72].

The SS1 samples consistently contain a significantly higher content

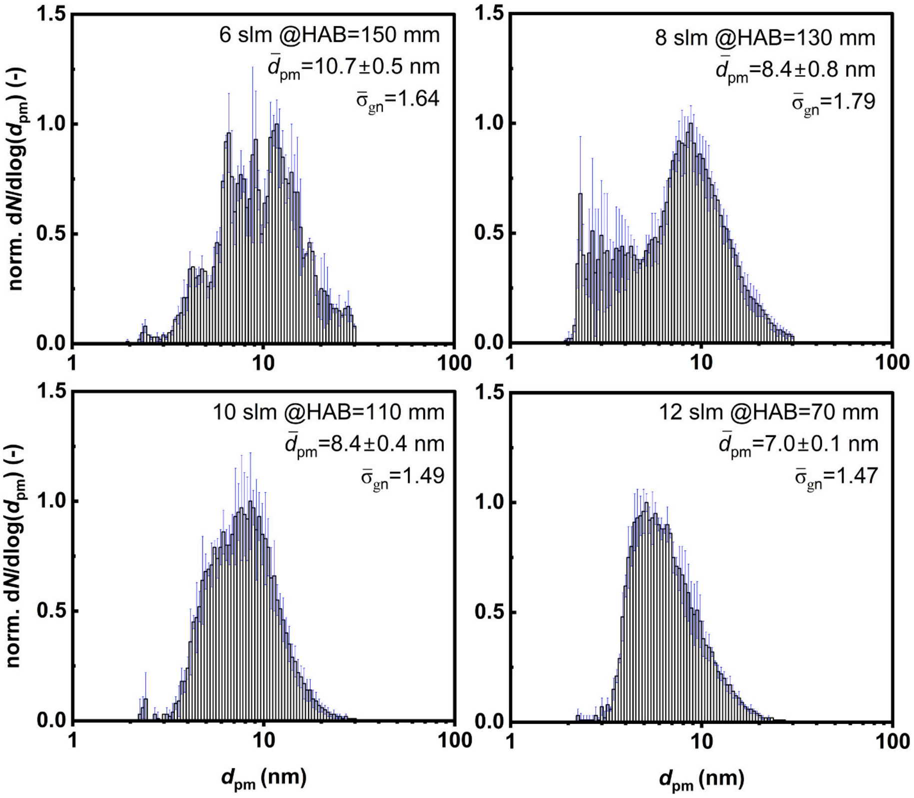

Fig. 7. Normalized particle size distribution measured at HAB, corresponding to the abrupt agglomerate growth observed in SS1 burner.

of unburned hydrocarbons, indicating comparatively incomplete combustion, as supported by PDA data. The exothermic DSC signals further evidence this, and the temperature range over which the exothermic reaction is observed is significantly wider than that for the SS2 samples. The mass spectra at $m/z = 44$ (CO_2) and 18 (H_2O), together with the exothermic DSC signal, support this. The total mass losses of all samples displayed in Fig. 8b indicate that the residual content in SS1 samples increases from 15 to 29 wt% while DG flow increases from 6 to 12 slm. In contrast, the residual content in the SS2 samples only rises from 12 to 19 wt%. However, the difference in mass losses between the two burners is relatively small for the DG flow range of 6 – 10 slm. An increased DG flow results in shorter residence time and cooler reaction conditions, leading to a higher amount of unburned residues. Beyond 400 °C, all remaining residues are lost. However, a slight increase in mass starting from 500 °C may be attributed to the oxidation of magnetite (Fe_3O_4) to Fe_2O_3.

The mass losses related to the release of H_2O/HNO_3 and carbonaceous byproducts are presented in Fig. 8c and d, respectively. SS1 samples exhibit significantly lower impurity levels from the absorbed H_2O/HNO_3, likely due to reduced specific surface area. However, SS1 samples also contain significantly greater amounts of carbonaceous residues. The lower flame activity within the spray flame impacts the amount of carbonaceous residues [40,72].

In summary, the total mass loss of the samples studied ranges from

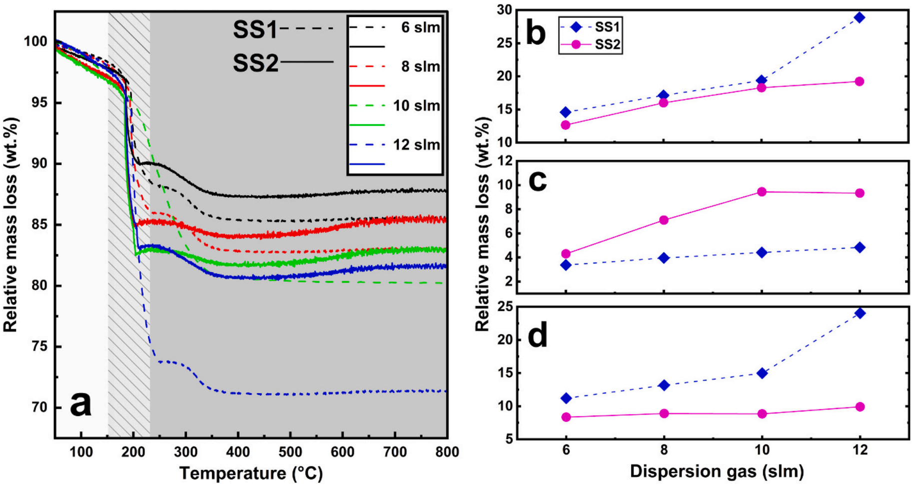

Fig. 8. Relative mass losses of samples obtained from TGA measurements. (a) The evolution of the relative mass losses of samples produced by both burners during thermal treatment across all dispersion gas flows. (b) Final mass losses of each sample after TGA. (c) Relative mass losses related to water and nitric acid in the temperature range ~37 – 185 °C, (d) pertaining to carbonaceous residues in the temperature range ~185 – 400 °C.

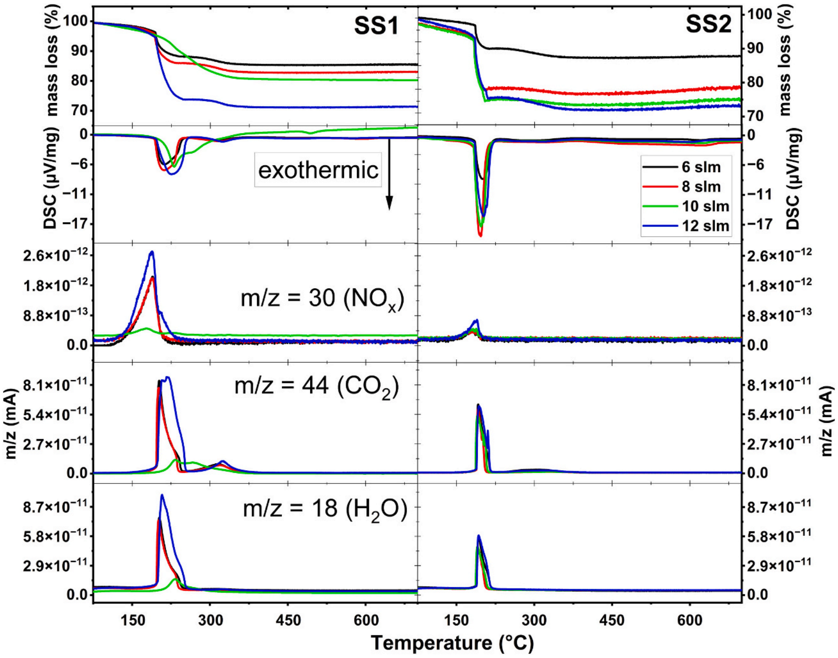

Fig. 9. Species evolution in the air atmosphere recovered during thermal treatment with a mass spectrometer across all dispersion gas flows with corresponding relative mass losses and DSC signals.

12 to 29 wt%. These values align with some reported in the literature for various metal oxides produced via SFS, 13 wt% [4], 2.2 – 37.6 wt% [23], 14 – 18 wt% [40], and 10 – 35 wt% [79]. The residual content in the powder is affected by the material chemistry (use of low-volatile 2-ethylhexanoic acid), spray flame characteristics (droplet size and high-temperature residence time), and flame activity.

After evaluating the remaining residual content in the samples, the next section discusses the relationship between operating process conditions and properties such as specific surface area and primary particle size.

3.5.2. Raman spectroscopy

Raman spectroscopy was used to identify qualitatively the crystalline phases of iron oxide nanoparticles (magnetite, hematite, and maghemite). These phases display characteristic peaks within the wavelength range of 150 – 850 cm^{-1} [21,79–83]. To interpret the spectra of the samples studied here, reference spectra from the work of Faria et al. [84] were used. The reference spectra depicted in Fig. 10a align well with several studies found in the literature, according to our previous work [44]. The measured spectra of the samples are shown in Fig. 10b and c. Three peaks at approximately 710, 510, and 365 cm^{-1} match well with the maghemite reference peak positions. Therefore, Raman spectroscopy indicates that predominantly maghemite was synthesized in both burners.

Recent advancements in SFS enable the precise control of the iron oxide oxidation state and polymorphism by tailoring process conditions. Despite the high temperatures in spray flames, the inherently short

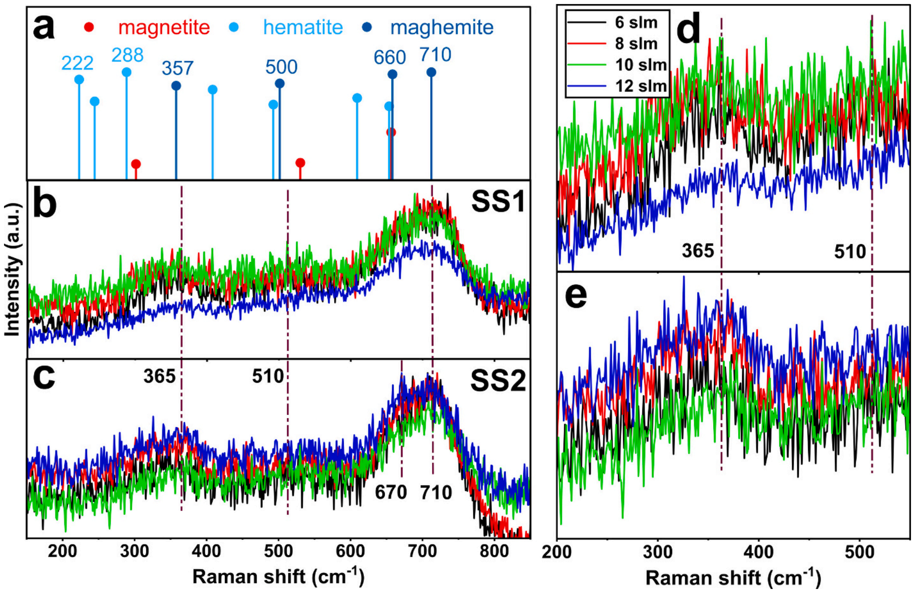

Fig. 10. (a) Reference positions of Raman active vibrations of magnetite, maghemite, and hematite according to [84]. (b) and (c) Raman spectra of iron oxide samples produced by SS1 and SS2, respectively. (d) and (e) Magnifications of (b) and (c) in the range 200 – 600 cm^{-1}, respectively.

residence times in SFS facilitate the synthesis of metastable γ-Fe_2O_3 [85]. Several studies have investigated the impact of oxygen content during SFS on the oxidation state and phase composition of iron oxides [21,23,44,82,83]. Notably, Strobel and Pratsinis [21] conducted a systematic study on how atmospheric conditions during the SFS of iron oxide can be used to control the final oxidation state of nanoparticles. Using a mixture of EtOH and EHA and $Fe(NO_3)_3{\cdot}9H_2O$ as the precursor solution, pure γ-Fe_2O_3 is synthesized in an open combustion burner at lower equivalence ratios (ϕ <0.87). Since ϕ was varied in this study in the range of 0.24 – 0.31 and according to Raman spectra of the powders, the synthesis of pure γ-Fe_2O_3 nanoparticles is assumed. Although a slight mass increase (1 – 2 wt%) is observed during TGA above 500 °C, as shown in Fig. 6a by some samples, suggesting the potential presence of small amounts of Fe_3O_4.

3.5.3. Size distribution and morphology of primary particles

As mentioned above, previous studies [35,44] have already demonstrated that the SS2 nozzle produces not only finer droplets but also finer particles. This is consistent with our results, as shown in Fig. 9. Increasing the dispersion gas flow results in higher specific surface areas (*SSA*) caused by shorter particle residence times in the high-temperature zone. As a result, the sintering rate is reduced. In addition, the particle

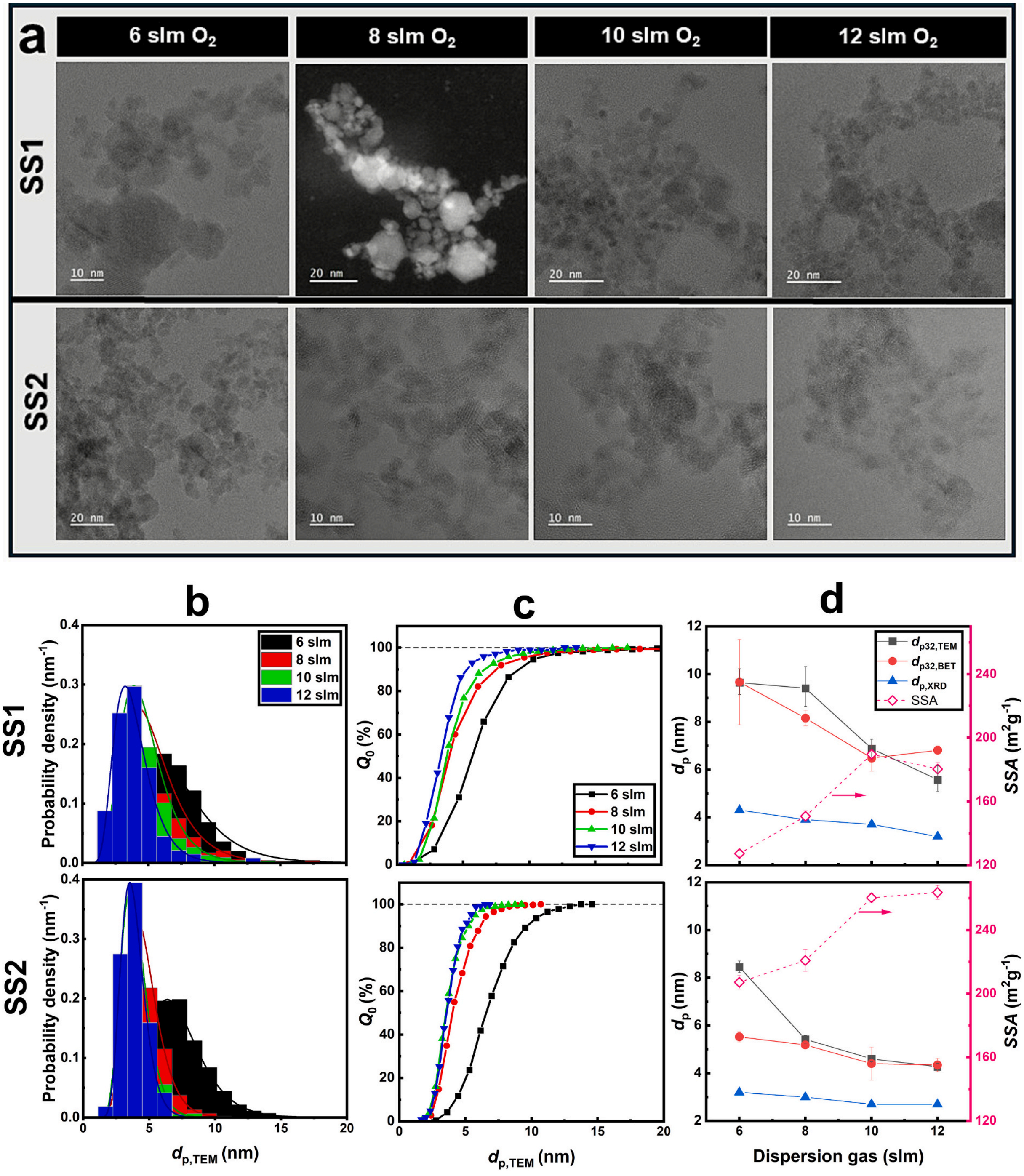

Fig. 11. (a) TEM micrographs of each powder. (b) Number-based primary particle size density distributions and (c) corresponding cumulative distributions obtained from TEM image analysis. (d) BET specific surface areas and Characteristic mean particle diameters with respect to dispersion gas flow: Sauter mean diameters obtained from BET and TEM (with 95 % confidence interval), mean crystallite size obtained from Rietveld analysis of XRD.

collision frequency decreases owing to the gas dilution (DG flow and air entrainment). Consequently, the agglomeration/aggregation kinetics also decrease. TEM/HRTEM analysis of the samples was conducted to gain insight into the synthesis pathways, morphology, and primary particle (PP) size. Fig. 9a shows the micrographs of the powders, synthesized with both burners, collected from the filter surface. Polydisperse (spherical-like) primary particles were produced predominantly at each process condition. However, some medium-sized particles in the range $20 - 30$ nm and dense particles are also present. The lower statistical count of larger particles suggests that gas-to-particle conversion predominates over droplet-to-particle conversion, which typically results in particles exceeding 100 nm. Very few of such large particles could be observed on TEM images (see supplementary materials, Fig. S3). Fast Fourier Transformation (FFT) analysis of single-particle TEM diffraction patterns confirms the crystallinity of samples (see Fig. 12c and d). However, distinguishing γ-Fe_2O_3 from Fe_3O_4 by TEM/HRTEM was challenging because their crystal lattice plane distances are nearly identical. Therefore, the assumption made in Section 3.4.2 prevails. It is essential to note that HRTEM and the associated FFT measurements are inherently selective and do not provide statistically representative information about the entire particle ensemble. Consequently, other phases and/or amorphous particles cannot be completely ruled out.

However, micrographs remain a reliable method for gaining insight into primary particle size, their distribution, and structure. A number of $416 - 1036$ primary particles were counted and measured on several TEM images at each process condition to ensure reasonable statistical reliability of the results. Fig. 11b and c display number-based primary particle size distributions in the form of histograms and cumulative distributions for both burners. The Sauter mean diameter of primary particles was calculated from the size distributions and compared to the respective size obtained from BET measurements in Fig. 9d. The mean crystallite size from Rietveld analysis of XRD measurements (see section 3.4.4) is also plotted for each flow condition. Generally, the primary particle size clearly decreases as the dispersion gas flow increases. When increasing from 6 to 12 slm, the primary particle size is reduced by approximately half (considering $d_{\mathrm{p32,TEM}}$ from 9.66 to 5.77 nm for SS1 and 8.45 to 4.24 nm for SS2). The $d_{\mathrm{p32,TEM}}$ and $d_{\mathrm{p32,BET}}$ show a fairly good agreement. When comparing these values, it should be noted that the plotted confidence intervals account only for statistical errors arising from limited sample size and do not include systematic errors.

In conclusion, increasing the dispersion gas flow rate lowers the flame temperature, shifting the particle growth mechanisms from sintering and aggregation-dominated (hard-agglomerates) to sintering-limited and agglomeration-dominated (soft-agglomerates) process. A stronger cooling effect significantly reduces the sintering rate while promoting the dominant agglomeration of particles, resulting in larger agglomerates composed of weakly agglomerated aggregates.

The geometric standard deviation $\sigma_{\mathrm{gn,PP}}$ of SS1 in Table 3 shows a relatively broader primary particle size distribution (PPSD) and appears not to be affected by DG flow, as its value remains roughly constant. The one for SS2 decreases with increasing DG flow, ranging from 1.34 to 1.27. These values are in line with reported investigations for SFS [10,47,60,86]. Eggersdorfer and Pratsinis [87] have investigated numerically the effect of primary particle polydispersity on the mass fractal dimension (D_f) of agglomerates formed by several collision mechanisms. Goudeli et al. [88] did a similar study in the free molecular regime, focusing on the growth of coagulating agglomerates. The main finding of these studies is that a broader PPSD (higher $\sigma_{\mathrm{gn,PP}}$) leads to elongated and open agglomerates, corresponding to lower D_f. Increasing $\sigma_{\mathrm{gn,PP}}$ does not alter the final asymptotic values of D_f, but it delays the attainment of self-preserving size distribution (SPSD) during agglomeration [88].

For example, at 6 slm DG, the D_f is estimated, according to [87] for diffusion-limited particle-cluster agglomeration, to be ~2.21 for $\sigma_{\mathrm{gn,PP}} = 1.46$, and ~2.30 for $\sigma_{\mathrm{gn,PP}} = 1.34$, for SS1 and SS2, respectively. As a result, both burners produce compact particles rather than fractal-like ones. Agglomerates undergoing coagulation in the free molecular regime attain their SPSD faster with decreasing D_f [89,90]. The number-based geometric standard deviation of SPSDs corresponds to 1.61 for $D_f = 2$ with $\tau = 3.24$, and 1.46 for $D_f = 3$ with $\tau = 4.31$ (τ represents the time needed for monodisperse particles to reach SPSD) [90]. Based on the knowledge of PP polydispersity, a better understanding of $\sigma_{\mathrm{gn,SMPS}}$ in Fig. 5b and d is gained. The higher polydispersity of PPs observed in SS1, due to the higher sintering rate and late precursor release, results in accelerated agglomeration of iron oxide nanoparticles but a delayed attainment of SPSD. This delay is suppressed at higher DG flow.

Sintered aggregates exhibit geometric standard deviations falling between the SPSD limit of pure agglomerates ($\sigma_{\mathrm{gn,m}} = 2.03$ [88]) and perfect spheres ($\sigma_{\mathrm{gn}} = 1.46$ [90]) in the free molecular regime. When the agglomeration rate exceeds the sintering rate, $\sigma_{\mathrm{gn,m}}$ increases but remains below 1.75 [91]. The $\sigma_{\mathrm{gn,SMPS}}$ values of both burners tend toward 1.5 at 170 mm HAB, except for 6 slm SS1, which aligns with measurements typically reported in the literature for the SFS of different metal oxides with similar burners [10,59,60,86,92]. The high temperature reported in SFS facilitates the formation of compact particles, subsequently narrowing the particle size distribution [91]. The compact but non-spherical agglomerates ($D_f < 3$) produced in this study were reported in [44,45]. In these investigations, TEM analysis of thermophoretic samples from both burners (10 slm DG flow) revealed that the samples consisted mainly of compact iron oxide nanoparticles with a weakly aggregated structure, formed within the flame. This supports the self-preserving character observed in the SMPS data of this work. Such thermophoretic sampling was not performed in this study due to the wide parameter range investigated.

Table 3
Characteristic mean and median diameters obtained from TEM image analysis and corresponding number-based geometric standard deviation.

DG / slm	$d_{\mathrm{p10,TEM}}$ / nm	$\sigma_{\mathrm{gn,PP}}$ / -	$d_{\mathrm{p32,TEM}}$ / nm	$d_{\mathrm{p50,TEM}}$ / nm	# of PPs
SS1					
6	7.12 ± 0.20	1.46	9.65	5.70	858
8	5.39 ± 0.16	1.53	9.41	3.96	826
10	4.77 ± 0.12	1.46	6.88	3.77	964
12	3.96 ± 0.15	1.46	5.57	3.33	416
SS2					
6	7.24 ± 0.13	1.34	8.45	6.57	1036
8	4.57 ± 0.09	1.33	5.42	4.03	870
10	3.96 ± 0.07	1.30	4.60	3.54	800
12	3.84 ± 0.09	1.27	4.27	3.58	429

3.5.4. XRD analysis

XRD analysis was employed as an ensemble method to complement the primary particle size measurements from TEM and BET, as well as the phase identification from Raman spectroscopy. All samples revealed a predominant maghemite phase (Hermann-Mauguin space group symbol $Fd\bar{3}m$; COD code 9006316 [93]). A Rietveld analysis of the peak shapes clearly indicates a bimodal distribution of crystallite sizes. Since the morphological particle characterization (see previous section and Fig. 12a) already indicated a small number of significantly larger particles, a bimodal crystallite size of the maghemite phase was fitted to the measurement results by using two identical COD data sets in the Rietveld refinement [94,95]. It should be noted that XRD, like BET analysis, yields a mass-weighted average, whereas TEM image analysis yields a number-based average. This results in a significant impact of a few large crystallites on the mass-weighted size distribution of the whole crystallites. A comparative graphical representation of the measurements and the fit result of a sample produced by SS1 at 6 slm is demonstrated in Fig. 13a. The fit clearly indicates two distinct crystallite sizes with a

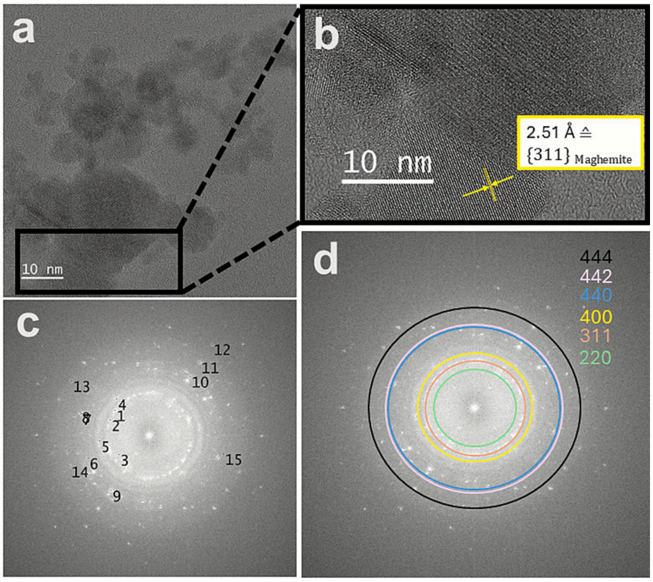

Fig. 12. (a) Exemplary HRTEM micrograph of the sample made by SS1 at 6 slm dispersion gas. (b) Magnification of (a) with calculated d-space of 2.51 Å for maghemite γ-Fe_2O_3. (c) and (d) represent Fast Fourier Transform (FFT) analysis of HRTEM image of small primary particles, revealing crystal lattice plane distances corresponding to γ-Fe_2O_3 (and Fe_3O_4).

Table 4
Summary of Rietveld refinements. DG, $d_{p,XRD}$ and Rwp represent the dispersion gas flow, crystallite size and R-factor weighted profile, respectively.

DG / slm	Rwp / %	Mass fraction *maghemite large* wt%	$d_{p,XRD,large}$ / nm	$d_{p,XRD,small}$ / nm
SS1				
6	4.03	12.2 ± 1.2	30 ± 5	4.3 ± 0.1
8	4.03	11.3 ± 1.0	30 ± 4	3.9 ± 0.1
10	4.34	11.4 ± 0.5	30 ± 2	3.7 ± 0.1
12	4.17	6.4 ± 0.4	29 ± 6	3.2 ± 0.1
SS2				
6	4.24	3.2 ± 0.5	57 ± 12	3.2 ± 0.1
8	3.63	5.2 ± 0.3	57 ± 8	3.0 ± 0.1
10	3.47	4.4 ± 0.3	63 ± 9	2.7 ± 0.1
12	3.68	6.2 ± 0.3	60 ± 8	2.7 ± 0.1

mean crystallite size $d_{p,XRD,small}$ of around 4 nm (blue area) and a mean crystallite size $d_{p,XRD,large}$ of roughly 30 nm (orange area). Notably, the width of the peak located at 34° strongly suggested a significant amorphous content in all samples, which was incorporated into the background signal for each Rietveld refinement (grey area in Fig. 13a). The superposition of this broad background peak with the primary maghemite diffraction peaks introduces some level of uncertainty in the analysis, potentially affecting the precision of the quantitative result. Fig. 13b and c compare diffractograms and fits for samples prepared at 6 and 12 slm dispersion gas flow rates for SS1 and SS2, respectively, highlighting the influence of synthesis parameters on the two crystallite ensembles, particularly evident in the differing intensities of the small peaks. The results of all Rietveld refinements regarding mass fraction and crystallite size are summarized in Table 4.

The analysis reveals several trends: comparing the two different burner configurations, $d_{p,XRD,small}$ varies only slightly ($\sim$3 nm compared to $\sim$4 nm at 6 slm for SS2 and SS1, respectively) while $d_{p,XRD,large}$ increased from about 30 nm for samples prepared with SS1 to roughly 60 nm for SS2 samples. However, nanopowders produced with SS2 generally showed a significantly lower weight fraction of large crystallites (3 – 6 wt%) than those from with SS1 (11 – 12 wt%). Furthermore, increasing the dispersion gas flow from 6 to 12 slm leads to a gradual decrease in $d_{p,XRD,small}$ by 1 nm for SS1 and 0.5 nm for SS2. In contrast, $d_{p,XRD,large}$ stays unaffected mainly in this parameter range. These trends in crystallite size are consistent with the BET and TEM data, supporting the observation that particle size decreases with increasing DG flow and that SS2 nanopowders generally contain a lower volume fraction of large particles compared to those made with SS1.

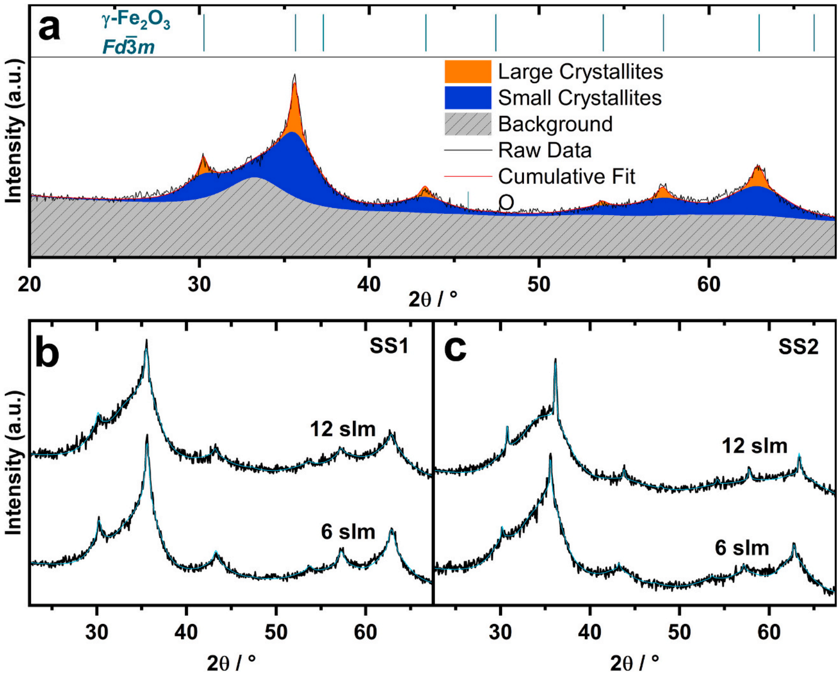

Fig. 13. XRD measurements of samples prepared by both burners at 6 and 12 slm, respectively: (a) Graphical analysis of SS1 at 6 slm showing the bimodal crystallite size distribution. (b, c) Direct comparison of measured XRD signal and final fits.

4. Conclusion

This study provides a detailed investigation of the impact of dispersion gas (DG) flow rate on spray flame synthesis (SFS) of iron oxide nanoparticles using two standardized *SpraySyn* burner configurations, SS1 and SS2. By systematically varying the dispersion gas flow rate (6 – 12 slm) and employing a suite of in-situ and ex-situ characterization techniques (PDA, HiaT-SMPS, Schlieren and OH*/CH* imaging, TGA-DSC-MS, BET, TEM, Raman, and XRD), a detailed understanding of atomization dynamics, flame behavior, and related nanoparticle evolution along the flame axis was achieved. Higher dispersion flow rates enhanced atomization efficiency, reduced mean droplet sizes, and intensified turbulent mixing. However, they simultaneously resulted in shorter high-temperature particle/droplet residence times and cooler flame cores. These effects directly influenced aggregate/agglomerate evolution by reducing sintering rates, resulting in smaller primary particles. SS2 consistently outperformed SS1 in producing finer, more homogeneous nanoparticles, owing to its angular nozzle geometry, which minimized flame pulsations and enhanced flame stability. The evolution of agglomerate size in SS1 exhibits spontaneous, significantly larger agglomerates outside the flame, attributed to late droplet evaporation and precursor release in combination with flow recirculation zones.

Analysis of primary particle size by TEM reveals broader distributions in SS1, resulting from later particle formation, which accelerates agglomeration but delays the attainment of self-preserving size distributions. In contrast, SS2 exhibits narrower distributions and faster attainment of a self-preserving size distribution across all flow conditions. Thermal analysis of samples revealed higher carbonaceous content in SS1. Raman and XRD confirmed maghemite (γ-Fe_2O_3) as the dominant phase across all conditions, with variations in crystallite size and bimodal phase fractions depending on burner type and dispersion gas flow.

The results emphasize the importance of dispersion gas flow and burner design in controlling particle size, morphology, and structural properties, such as polydispersity and fractal dimension. These findings offer valuable experimental data for future model validation and process optimization in flame-based nanoparticle synthesis.

CRediT authorship contribution statement

Orlando Massopo: Writing – original draft, Visualization, Validation, Methodology, Investigation, Formal analysis, Data curation, Conceptualization. **Ricardo Tischendorf:** Investigation, Conceptualization. **Munko Gonchikzhapov:** Methodology, Investigation. **Tina Kasper:** Supervision, Project administration. **Peter Augustin:** Writing – original draft, Methodology, Investigation, Conceptualization. **Burak Özer:** Investigation. **Manuel Reddemann:** Writing – review & editing, Conceptualization. **Reinhold Kneer:** Supervision, Project administration. **Mohammed-Ali Sheikh:** Software, Methodology, Investigation, Data curation. **Aydan Akyildiz Mert:** Data curation. **Hartmut Wiggers:** Writing – review & editing, Supervision, Project administration, Conceptualization. **Hans-Joachim Schmid:** Writing – review & editing, Supervision, Project administration, Conceptualization.

Declaration of competing interest

The authors declare the following financial interests/personal relationships which may be considered as potential competing interests.

Hans-Joachim Schmid reports financial support was provided by German Research Foundation. If there are other authors, they declare that they have no known competing financial interests or personal relationships that could have appeared to influence the work reported in this paper.

Acknowledgements

We kindly thank the German Research Foundation for funding through the project number 375857587 (SPP1980), including SCHM 1429/13-1, KN 764/20-1, Pl 368/19-1 and the project number 523959480 (SPP2419). We also thank Kristina Duschik (Department of Material Science, Paderborn University) for the electron microscopy analysis and constructive discussions, and the Department of Physics from Paderborn University for providing the necessary infrastructure to perform these analyses.

The X-ray data were collected using the Rigaku Smartlab High Resolution X-ray diffractometer of the Nanoparticle Processing Technology (NPPT) group (Prof. Markus Winterer) at the University of Duisburg-Essen. The instrument is funded through the DFG, Instrument proposal INST 20876/395-1, FUGG Project number 450350889, and the state of North Rhine-Westphalia, Germany.

Appendix A. Supplementary data

Supplementary data to this article can be found online at https://doi.org/10.1016/j.powtec.2025.121992.

Data availability

The data will be made available on request.

References

[1] W.Y. Teoh, R. Amal, L. Mädler, Flame spray pyrolysis: an enabling technology for nanoparticles design and fabrication, Nanoscale 2 (8) (2010) 1324–1347, https://doi.org/10.1039/c0nr00017e.

[2] R. Strobel, S.E. Pratsinis, Flame aerosol synthesis of smart nanostructured materials, J. Mater. Chem. 17 (45) (2007) 4743, https://doi.org/10.1039/b711652g.

[3] R. Koirala, S.E. Pratsinis, A. Baiker, Synthesis of catalytic materials in flames: opportunities and challenges, Chem. Soc. Rev. 45 (11) (2016) 3053–3068, https://doi.org/10.1039/c5cs00011d.

[4] F. Meierhofer, H. Li, M. Gockeln, R. Kun, T. Grieb, A. Rosenauer, et al., Screening precursor-solvent combinations for $Li_4Ti_5O_{12}$ energy storage material using flame spray pyrolysis, ACS Appl. Mater. Interfaces 9 (43) (2017) 37760–37777, https://doi.org/10.1021/acsami.7b11435.

[5] M. Gockeln, S. Pokhrel, F. Meierhofer, J. Glenneberg, M. Schowalter, A. Rosenauer, et al., Fabrication and performance of $Li_4Ti_5O_{12}$/C Li-ion battery electrodes using combined double flame spray pyrolysis and pressure-based lamination technique, J. Power Sources 374 (2018) 97–106, https://doi.org/10.1016/j.jpowsour.2017.11.016.

[6] L. Mädler, A. Roessler, S.E. Pratsinis, T. Sahm, A. Gurlo, N. Barsan, et al., Direct formation of highly porous gas-sensing films by in situ thermophoretic deposition of flame-made Pt/SnO_2 nanoparticles, Sens. Actuators B 114 (1) (2006) 283–295, https://doi.org/10.1016/j.snb.2005.05.014.

[7] M. Estévez, M. Cicuéndez, J. Crespo, J. Serrano-López, M. Colilla, C. Fernández-Acevedo, et al., Large-scale production of superparamagnetic iron oxide nanoparticles by flame spray pyrolysis: in vitro biological evaluation for biomedical applications, J. Colloid Interface Sci. 650 (Pt A) (2023) 560–572, https://doi.org/10.1016/j.jcis.2023.07.009.

[8] J. Beltran-Huarac, Z. Zhang, G. Pyrgiotakis, G. DeLoid, N. Vaze, S.M. Hussain, et al., Development of reference metal and metal oxide engineered nanomaterials for nanotoxicology research using high throughput and precision flame spray synthesis approaches, NanoImpact 10 (2018) 26–37, https://doi.org/10.1016/j.impact.2017.11.007.

[9] S. Pokhrel, L. Mädler, Flame-made particles for sensors, catalysis, and energy storage applications, Energy Fuel 34 (11) (2020) 13209–13224, https://doi.org/10.1021/acs.energyfuels.0c02220.

[10] F. Meierhofer, L. Mädler, U. Fritsching, Nanoparticle evolution in flame spray pyrolysis—process design via experimental and computational analysis, AICHE J. 66 (2) (2020), https://doi.org/10.1002/aic.16885.

[11] Q.A. Pankhurst, J. Connolly, S.K. Jones, J. Dodson, Application of magnetic nanoparticles in biomedicine, J. Phys. D 36 (13) (2003).

[12] S. Gul, S.B. Khan, I.U. Rehman, M.A. Khan, M.I. Khan, A comprehensive review of magnetic nanomaterials modern day Theranostics, Front. Mater. (2019) 6, https://doi.org/10.3389/fmats.2019.00179.

[13] A.K. Gupta, M. Gupta, Synthesis and surface engineering of iron oxide nanoparticles for biomedical applications, Biomaterials 26 (18) (2005) 3995–4021, https://doi.org/10.1016/j.biomaterials.2004.10.012.

[14] Q.A. Pankhurst, J. Connolly, S.K. Jones, J.J. Dobson, Applications of magnetic nanoparticles in biomedicine, J. Phys. D. Appl. Phys. 36 (13) (2003) R167, https://doi.org/10.1088/0022-3727/36/13/201.

[15] R. Strobel, S.E. Pratsinis, Effect of solvent composition on oxide morphology during flame spray pyrolysis of metal nitrates, Phys. Chem. Chem. Phys. 13 (20) (2011) 9246–9252, https://doi.org/10.1039/c0cp01416h.

[16] S. Tsantilis, S.E. Pratsinis, Soft- and hard-agglomerate aerosols made at high temperatures, Langmuir 20 (14) (2004) 5933–5939, https://doi.org/10.1021/la036389w.

[17] M.F.B. Stodt, M. Gonchikzhapov, T. Kasper, U. Fritsching, J. Kiefer, Chemistry of iron nitrate-based precursor solutions for spray-flame synthesis, Phys. Chem. Chem. Phys. 21 (44) (2019) 24793–24801, https://doi.org/10.1039/c9cp05007h.

[18] C.D. Rosebrock, N. Riefler, T. Wriedt, L. Mädler, S.D. Tse, Disruptive burning of precursor/solvent droplets in flame-spray synthesis of nanoparticles, AICHE J. 59 (12) (2013) 4553–4566, https://doi.org/10.1002/aic.14234.

[19] C.D. Rosebrock, T. Wriedt, L. Mädler, K. Wegner, The role of microexplosions in flame spray synthesis for homogeneous nanopowders from low-cost metal precursors, AICHE J. 62 (2) (2016) 381–391, https://doi.org/10.1002/aic.15056.

[20] R. Jossen, S.E. Pratsinis, W.J. Stark, L. Mädler, Criteria for flame-spray synthesis of hollow, Shell-like, or inhomogeneous oxides, J. Am. Ceram. Soc. 88 (6) (2005) 1388–1393, https://doi.org/10.1111/j.1551-2916.2005.00249.x.

[21] R. Strobel, S.E. Pratsinis, Direct synthesis of maghemite, magnetite and wustite nanoparticles by flame spray pyrolysis, Adv. Powder Technol. 20 (2) (2009) 190–194, https://doi.org/10.1016/j.apt.2008.08.002.

[22] L. Mädler, H.K. Kammler, R. Mueller, S.E. Pratsinis, Controlled synthesis of nanostructured particles by flame spray pyrolysis, J. Aerosol Sci. 33 (2) (2002) 369–389, https://doi.org/10.1016/S0021-8502(01)00159-8.

[23] Y. Li, Y. Hu, G. Huang, C. Li, Metallic iron nanoparticles: flame synthesis, characterization and magnetic properties, Particuology 11 (4) (2013) 460–467, https://doi.org/10.1016/j.partic.2012.10.008.

[24] M. Bieber, R. Tischendorf, H.-J. Schmid, M.A. Reddemann, R. Kneer, Influence of Precursor Concentration on Spray and Particle Formation in Flame Spray Pyrolysis, ILASS-Europe, Paris, France, 2019.

[25] F. Schneider, S. Suleiman, J. Menser, E. Borukhovich, I. Wlokas, A. Kempf, et al., SpraySyn-A standardized burner configuration for nanoparticle synthesis in spray flames, Rev. Sci. Instrum. 90 (8) (2019) 85108, https://doi.org/10.1063/1.5090232.

[26] DFG - GEPRIS - SPP 1980: Nanoparticle Synthesis in Spray Flames: Spray Syn: Measurement, Simulation, Processes, Available from: https://gepris.dfg.de/gepris/projekt/312959688?language=en, April 07, 2025.

[27] F. Fröde, T. Grenga, S. Dupont, R. Kneer, R. Tischendorf, O. Massopo, et al., Large eddy simulation of iron oxide formation in a laboratory spray flame, Applicati. Energy Combustion Sci. 16 (2023) 100191, https://doi.org/10.1016/j.jaecs.2023.100191.

[28] P. Bianchi Neto, F. Meierhofer, H.F. Meier, U. Fritsching, D. Noriler, Modelling polydisperse nanoparticle size distributions as produced via flame spray pyrolysis, Powder Technol. 370 (2020) 116–128, https://doi.org/10.1016/j.powtec.2020.05.019.

[29] L. Buss, F. Meierhofer, P. Bianchi Neto, H. França Meier, U. Fritsching, D. Noriler, Impact of co-flow on the spray flame behaviour applied to nanoparticle synthesis, Can. J. Chem. Eng. 97 (2) (2019) 604–615, https://doi.org/10.1002/cjce.23386.

[30] S. Karaminejad, S.M. Dupont, M. Bieber, M.A. Reddemann, R. Kneer, T. Dreier, et al., Characterization of spray parameters and flame stability in two modified nozzle configurations of the SpraySyn burner, Proc. Combust. Inst. 39 (2) (2023) 2673–2682, https://doi.org/10.1016/j.proci.2022.07.248.

[31] S.-J. Baik, P. Wollny, M. Nanjaiah, I. Wlokas, A. Kempf, Large eddy simulation of iron(III) oxide nanoparticle synthesis in spray flames, Applicati. Energy Combustion Sci. 15 (2023) 100185, https://doi.org/10.1016/j.jaecs.2023.100185.

[32] F. Fröde, O. Desjardins, M. Bieber, M. Reddemann, R. Kneer, H. Pitsch, Multiscale simulation of spray and mixture formation for a coaxial atomizer, Int. J. Multiphase Flow 182 (2025) 104971, https://doi.org/10.1016/j.ijmultiphaseflow.2024.104971.

[33] A. Rittler, L. Deng, I. Wlokas, A.M. Kempf, Large eddy simulations of nanoparticle synthesis from flame spray pyrolysis, Proc. Combust. Inst. 36 (1) (2017) 1077–1087, https://doi.org/10.1016/j.proci.2016.08.005.

[34] J. Sellmann, P. Wollny, S.-J. Baik, S. Suleiman, F. Schneider, C. Schulz, et al., LES of nanoparticle synthesis in the spraysyn burner: a comparison against experiments, Powder Technol. 404 (2022) 117466, https://doi.org/10.1016/j.powtec.2022.117466.

[35] M. Bieber, M. Al-Khatib, F. Fröde, H. Pitsch, M.A. Reddemann, H.-J. Schmid, et al., Influence of angled dispersion gas on coaxial atomization, spray and flame formation in the context of spray-flame synthesis of nanoparticles, Exp. Fluids 62 (5) (2021), https://doi.org/10.1007/s00348-021-03196-6.

[36] M. Stodt, J.D. Groeneveld, L. Mädler, J. Kiefer, U. Fritsching, Microexplosions of multicomponent drops in spray flames, Combust. Flame 240 (2022) 112043, https://doi.org/10.1016/j.combustflame.2022.112043.

[37] M. Stodt, J. Kiefer, U. Fritsching, Impact of atomization and spray flow conditions on droplet μ -explosions and temporal self-similarity in the FSP process, Applicati. Energy Combustion Sci. 15 (2023) 100170, https://doi.org/10.1016/j.jaecs.2023.100170.

[38] M.F.B. Stodt, J. Kiefer, U. Fritsching, Drop dynamics in heterogeneous spray flames for nanoparticle synthesis, Atomiz Spr 30 (11) (2020) 779–797, https://doi.org/10.1615/AtomizSpr.2020034819.

[39] M.F.B. Stodt, J. Kiefer, U. Fritsching, Ethanol droplet formation, dynamics and combustion mode in the flame of the SpraySyn-nozzle, Exp. Fluids 60 (8) (2019), https://doi.org/10.1007/s00348-019-2771-9.

[40] R. Tischendorf, K. Duschik, F. Fröde, M. Reddemann, R. Kneer, H. Pitsch, et al., On the formation of carbonaceous by-product species in spray flame synthesis of maghemite nanoparticles, Appl. Sci. 15 (6) (2025) 3294, https://doi.org/10.3390/app15063294.

[41] F.J. Martins, C.T. Foo, A. Unterberger, S. Karaminejad, T. Endres, K. Mohri, Analyzing 3D fields of refractive index, emission and temperature in spray-flame nanoparticle synthesis via tomographic imaging using multi-simultaneous measurements (TIMes), Applicati. Energy Combustion Sci. 16 (2023) 100213, https://doi.org/10.1016/j.jaecs.2023.100213.

[42] A. Kumar, J. Kirchmann, F. Beyrau, A. Kronenburg, Jet flapping and its effect on flame oscillations in the SPP1980 SpraySyn burner, Exp. Thermal Fluid Sci. 142 (2023) 110826, https://doi.org/10.1016/j.expthermflusci.2022.110826.

[43] P. Lang, N.E. Schneider, F.J. Huber, S. Will, Characterization of the SpraySyn 2.0 burner: droplet diameters, flame stability and particle sizes. Applications in energy and combustion, Science 22 (2025) 100324, https://doi.org/10.1016/j.jaecs.2025.100324.

[44] R. Tischendorf, O. Massopo, O. Prymak, S. Dupont, F. Fröde, H. Pitsch, et al., Maghemite nanoparticles synthesis via spray flame synthesis and particle characterization by hole in a tube sampling and scanning mobility particle sizing (HIAT-SMPS), Applicati. Energy Combustion Sci. 17 (2024) 100235, https://doi.org/10.1016/j.jaecs.2023.100235.

[45] R. Tischendorf, M. Simmler, C. Weinberger, M. Bieber, M. Reddemann, F. Fröde, et al., Examination of the evolution of iron oxide nanoparticles in flame spray pyrolysis by tailored in situ particle sampling techniques, J. Aerosol Sci. 154 (2021) 105722, https://doi.org/10.1016/j.jaerosci.2020.105722.

[46] A.J. Gröhn, S.E. Pratsinis, A. Sánchez-Ferrer, R. Mezzenga, K. Wegner, Scale-up of nanoparticle synthesis by flame spray pyrolysis: the high-temperature particle residence time, Ind. Eng. Chem. Res. 53 (26) (2014) 10734–10742, https://doi.org/10.1021/ie501709s.

[47] A.J. Gröhn, S.E. Pratsinis, K. Wegner, Fluid-particle dynamics during combustion spray aerosol synthesis of ZrO2, Chem. Eng. J. 191 (2012) 491–502, https://doi.org/10.1016/j.cej.2012.02.093.

[48] C. Wu, Y. Zhang, L. Yang, B. Xiao, A. Jiao, K. Li, et al., Flame spray pyrolysis synthesis of WO3 sensing materials: effects of flame parameters on particle size distribution and NO2 sensing performance, Langmuir 38 (50) (2022) 15506–15515, https://doi.org/10.1021/acs.langmuir.2c01945.

[49] Cornell RM, Schwertmann U, others. The iron Oxides: Structure, Properties, Reactions, Occurrences, and Uses. Wiley-vch Weinheim; 2003.

[50] Y. El Mendili, J.-F. Bardeau, N. Randrianantoandro, F. Grasset, J.-M. Greneche, Insights into the mechanism related to the phase transition from γ-Fe_2O_3 to α-Fe_2O_3 nanoparticles induced by thermal treatment and laser irradiation, J. Phys. Chem. C 116 (44) (2012) 23785–23792, https://doi.org/10.1021/jp308418x.

[51] M. Krispin, A. Ullrich, S. Horn, Crystal structure of iron-oxide nanoparticles synthesized from ferritin, J. Nanopart. Res. 14 (2) (2012), https://doi.org/10.1007/s11051-011-0669-4.

[52] U. Schwertmann, R.M. Cornell, Iron Oxides in the Laboratory: Preparation and Characterization, John Wiley & Sons, 2008.

[53] G. Pitcher, G. Wigley, M. Saffman, Sensitivity of dropsize measurements by phase doppler anemometry to refractive index changes in combusting fuel sprays, in: Applications of Laser Techniques to Fluid Mechanics: 5th International Symposium Lisbon, Portugal, 9–12 July, 1990, 1991, pp. 227–247.

[54] C.T. Foo, A. Unterberger, J.W.A. Martins Fabio, M.M. Prenting, C. Schulz, K. Mohri, Investigating spray flames for nanoparticle synthesis via tomographic imaging using multi-simultaneous measurements (TIMes) of emission, Opt. Express 30 (9) (2022) 15524–15545, https://doi.org/10.1364/OE.449269.

[55] S. Karaminejad, A. El Moussawi, T. Dreier, T. Endres, C. Schulz, Multi-line OH-LIF for gas-phase temperature and concentration imaging in the SpraySyn burner, Applicati. Energy Combustion Sci. 16 (2023) 100222, https://doi.org/10.1016/j.jaecs.2023.100222.

[56] M. Orain, Y. Hardalupas, Effect of fuel type on equivalence ratio measurements using chemiluminescence in premixed flames, Comptes Rendus. Mécanique 338 (5) (2010) 241–254, https://doi.org/10.1016/j.crme.2010.05.002.

[57] M.M. Kamal, Two-line (CH^*/CO_2^*) chemiluminescence technique for equivalence ratio mapping in turbulent stratified flames, Energy 192 (2020) 116485, https://doi.org/10.1016/j.energy.2019.116485.

[58] S. Kook, M.K. Le, S. Padala, E.R. Hawkes, Z-type schlieren setup and its application to high-speed imaging of gasoline sprays, 2011.

[59] E. Goudeli, A.J. Gröhn, S.E. Pratsinis, Sampling and dilution of nanoparticles at high temperature, Aerosol Sci. Technol. 50 (6) (2016) 591–604, https://doi.org/10.1080/02786826.2016.1168922.

[60] A.J. Gröhn, M.L. Eggersdorfer, S.E. Pratsinis, K. Wegner, On-line monitoring of primary and agglomerate particle dynamics, J. Aerosol Sci. 73 (2014) 1–13, https://doi.org/10.1016/j.jaerosci.2014.03.001.

[61] A. Spyrogianni, I.K. Herrmann, K. Keevend, S.E. Pratsinis, K. Wegner, The silanol content and in vitro cytolytic activity of flame-made silica, J. Colloid Interface Sci. 507 (2017) 95–106, https://doi.org/10.1016/j.jcis.2017.07.096.

[62] VDI-Wärmeatlas: Mit 320 Tabellen, 11th ed., Springer Vieweg, Berlin, Heidelberg, 2013.

[63] S. Brunauer, P.H. Emmett, E. Teller, Adsorption of gases in multimolecular layers, J. Am. Chem. Soc. 60 (2) (1938) 309–319.

[64] S. Lowell, Characterization of Porous Solids and Powders: Surface Area, Pore Size and Density, Springer, Dordrecht, 2004.

[65] Iron (III) Oxide, Fe_2O_3 (Maghemite), Available from: https://www.matweb.com/search/DataSheet.aspx?MatGUID=b9347d6fe1d4463188c679e065f84e2f&ckck=1, April 09, 2025.

[66] Wayne Rasband, ImageJ-Image Processing and Analysis in Java [software], Available from: https://imagej.net/ij/index.html, December 12, 2024.

[67] W.C. Hinds, Y. Zhu, Aerosol Technology: Properties, Behavior, and Measurement of Airborne Particles, John Wiley & Sons, 2022.

[68] A. Peter, Ö. Burak, B. Malte, D. Sophie, E. Jacob, H. Lukas, et al., Dataset of combined OH/CH Narrowband and Schlieren Imaging with Phase-Doppler Anemometry for Spray Flame Synthesis in SpraySyn 1 and 2 under Varying Dispersion Gas Flows, 2025, https://doi.org/10.18154/RWTH-2025-03928.

[69] M.C. Heine, S.E. Pratsinis, Droplet and particle dynamics during flame spray synthesis of nanoparticles, Ind. Eng. Chem. Res. 44 (16) (2005) 6222–6232, https://doi.org/10.1021/ie0490278.

[70] M. Gonchikzhapov, T. Kasper, Thermal and chemical structure of ethanol and 2-ethylhexanoic acid/ethanol SpraySyn flames, Applicati. Energy Combustion Sci. 15 (2023) 100174, https://doi.org/10.1016/j.jaecs.2023.100174.

[71] C.M. Kennedy, M.J. Dunn, A.R. Masri, Flame stability characteristics of a flame spray pyrolysis burner, Combust. Flame 260 (2024) 113247, https://doi.org/10.1016/j.combustflame.2023.113247.

[72] C.M. Kennedy, Y. Zhang, S. Zou, M.J. Dunn, A.R. Masri, Influence of flame stability on iron oxide nanoparticle growth during FSP, J. Aerosol Sci. 183 (2025) 106475, https://doi.org/10.1016/j.jaerosci.2024.106475.

[73] F.P. Ricou, D.B. Spalding, Measurements of entrainment by axisymmetrical turbulent jets, 2025.

[74] L. Muniz, M.G. Mungal, Effects of heat release and buoyancy on flow structure and entrainment in turbulent nonpremixed flames, Combust. Flame 126 (1–2) (2001) 1402–1420, https://doi.org/10.1016/S0010-2180(01)00253-X.

[75] L. Sumathirathne, W.B. Euler, Catalysis of the thermal decomposition of transition metal nitrate hydrates by poly(vinylidene difluoride), Polymers (Basel) 13 (18) (2021), https://doi.org/10.3390/polym13183112.

[76] P. Melnikov, V.A. Nascimento, I.V. Arkhangelsky, L.Z. Zanoni Consolo, L.C.S. de Oliveira, Thermal decomposition mechanism of iron(III) nitrate and characterization of intermediate products by the technique of computerized modeling, J. Therm. Anal. Calorim. 115 (1) (2014) 145–151, https://doi.org/10.1007/s10973-013-3339-1.

[77] K. Wieczorek-Ciurowa, A. Kozak, The thermal decomposition of $Fe(NO_3)_3x9H_2O$, J. Therm. Anal. Calorim. 58 (3) (1999) 647–651, https://doi.org/10.1023/a:1010112814013.

[78] K. Deshpande, A. Mukasyan, A. Varma, Direct synthesis of Iron oxide Nanopowders by the combustion approach: reaction mechanism and properties, Chem. Mater. 16 (24) (2004) 4896–4904, https://doi.org/10.1021/cm040061m.

[79] L. Carvajal, R. Buitrago-Sierra, A. Santamaría, S. Angel, H. Wiggers, J. Gallego, Effect of spray parameters in a spray flame reactor during FexOy nanoparticles synthesis, J Therm Spray Tech 29 (3) (2020) 368–383, https://doi.org/10.1007/s11666-020-00991-1.

[80] D. Li, W.Y. Teoh, C. Selomulya, R.C. Woodward, P. Munroe, R. Amal, Insight into microstructural and magnetic properties of flame-made γ-Fe_2O_3 nanoparticles, J. Mater. Chem. 17 (46) (2007) 4876, https://doi.org/10.1039/b711705a.

[81] I.K. Herrmann, R.N. Grass, D. Mazunin, W.J. Stark, Synthesis and covalent surface functionalization of nonoxidic Iron Core−Shell nanomagnets, Chem. Mater. 21 (14) (2009) 3275–3281, https://doi.org/10.1021/cm900785u.

[82] M. Sorvali, M. Honkanen, L. Hyvärinen, R. Kuisma, J. Larjo, J.M. Mäkelä, Crystallographic phase formation of iron oxide particles produced from iron nitrate by liquid flame spray with a dual oxygen flow, Int J Ceramic Engine & Sci 3 (5) (2021) 227–236, https://doi.org/10.1002/ces2.10102.

[83] M. Sorvali, M. Nikka, P. Juuti, M. Honkanen, T. Salminen, L. Hyvärinen, et al., Controlling the phase of iron oxide nanoparticles fabricated from iron(III) nitrate by liquid flame spray, Int J Ceramic Engine & Sci 1 (4) (2019) 194–205, https://doi.org/10.1002/ces2.10025.

[84] de Faria, Ven&acirc, ncio Silva, de Oliveira, Raman microspectroscopy of some iron oxides and oxyhydroxides, 2025, https://doi.org/10.1002/(SICI)1097-4555(199711)28:11<873:AID-JRS177>3.0.CO;2-B.

[85] S. Grimm, M. Schultz, S. Barth, R. Muller, Flame pyrolysis-a preparation route for ultrafine pure γ-Fe_2O_3 powders and the control of their particle size and properties, J. Mater. Sci. 32 (4) (1997) 1083–1092, https://doi.org/10.1023/A:1018598927041.

[86] R. Mueller, R. Jossen, H.K. Kammler, S.E. Pratsinis, M.K. Akhtar, Growth of zirconia particles made by flame spray pyrolysis, AICHE J. 50 (12) (2004) 3085–3094, https://doi.org/10.1002/aic.10272.

[87] M.L. Eggersdorfer, S.E. Pratsinis, The structure of agglomerates consisting of polydisperse particles, Aerosol Sci. Technol. 46 (3) (2012) 347–353, https://doi.org/10.1080/02786826.2011.631956.

[88] E. Goudeli, M.L. Eggersdorfer, S.E. Pratsinis, Coagulation of agglomerates consisting of polydisperse primary particles, Langmuir 32 (36) (2016) 9276–9285, https://doi.org/10.1021/acs.langmuir.6b02455.

[89] E. Goudeli, M.L. Eggersdorfer, S.E. Pratsinis, Coagulation-agglomeration of fractal-like particles: structure and self-preserving size distribution, Langmuir 31 (4) (2015) 1320–1327, https://doi.org/10.1021/la504296z.

[90] S. Vemury, S.E. Pratsinis, Self-preserving size distributions of agglomerates, J. Aerosol Sci. 26 (2) (1995) 175–185, https://doi.org/10.1016/0021-8502(94)00103-6.

[91] M.L. Eggersdorfer, E. Goudeli, Structure and dynamics of fractal-like particles made by agglomeration and sintering, AICHE J. 66 (12) (2020), https://doi.org/10.1002/aic.17099.

[92] G.A. Kelesidis, F.M. Furrer, K. Wegner, S.E. Pratsinis, Impact of humidity on silica nanoparticle agglomerate morphology and size distribution, Langmuir 34 (29) (2018) 8532–8541, https://doi.org/10.1021/acs.langmuir.8b00576.

[93] Crystallography Open Database: Information card for entry 9006316, Available from: https://www.crystallography.net/cod/9006316.html, May 01, 2025.

[94] S. Angel, F. Schneider, S. Apazeller, W. Kaziur-Cegla, T.C. Schmidt, C. Schulz, et al., Spray-flame synthesis of $LaMO_3$ (M = Mn, Fe, co) perovskite nanomaterials: effect of spray droplet size and esterification on particle size distribution, Proc. Combust. Inst. 38 (1) (2021) 1279–1287, https://doi.org/10.1016/j.proci.2020.07.116.

[95] S. Hardt, I. Wlokas, C. Schulz, H. Wiggers, Impact of ambient pressure on titania nanoparticle formation during spray-flame synthesis, J. Nanosci. Nanotechnol. 15 (12) (2015) 9449–9456, https://doi.org/10.1166/jnn.2015.10607.